

X-ray Diagnostics of Thermal Conditions of the Hot Plasmas in the Centaurus Cluster

I. Takahashi¹, M. Kawaharada², K. Makishima^{1,2}, K. Matsushita³, Y. Fukazawa⁴, Y. Ikebe⁵,
T. Kitaguchi¹, M. Kokubun⁶, K. Nakazawa¹, S. Okuyama¹, N. Ota³, and T. Tamura⁶

*1: Department of Physics, University of Tokyo, 7-3-1 Hongo, Bunkyo-ku,
Tokyo 113-0011, Japan*

*2: Institute of Physical and Chemical Research (RIKEN), 2-1 Hirosawa, Wako,
Saitama 351-0198, Japan*

*3: Department of Physics, Tokyo University of Science, Kagurazaka, Shinjuku-ku,
Tokyo 162-8601, Japan*

*4: Department of Physical Science, School of Science, Hiroshima University,
1-3-1 Kagamiyama, Higashi-Hiroshima, Hiroshima 739-8526*

*5: National Museum of Emerging Science and Innovation, 2-41 Aomi, Koto-ku,
Tokyo 135-0064, Japan*

*6: Institute of Space and Astronautical Science, Japan Aerospace Exploration Agency,
2-1-1 Yoshinodai, Sagami-hara, Kanagawa 229-8510, Japan*

ABSTRACT

X-ray data of the Centaurus cluster, obtained with *XMM-Newton* for 45 ksec, were analyzed. Deprojected EPIC spectra from concentric thin shell regions were reproduced equally well by a single-phase plasma emission model, or by a two-phase model developed by *ASCA*, both incorporating cool (1.7–2.0 keV) and hot (~ 4 keV) plasma temperatures. However, EPIC spectra with higher statistics, accumulated over 3-dimensional thick shell regions, were reproduced better by the two-phase model than by the single-phase one. Therefore, hot and cool plasma phases are inferred to co-exist in the cluster core region within ~ 70 kpc. The iron and silicon abundances of the plasma were reconfirmed to increase significantly towards the center, while that of oxygen was consistent with being radially constant. The implied non-solar abundance ratios explain away the previously reported excess X-ray absorption from the central region. Although an additional cool (~ 0.7 keV) emission was detected within ~ 20 kpc of the center, the RGS data gave tight upper limits on any emission with a temperature

below ~ 0.5 keV. These results are compiled into a magnetosphere model, which interprets the cool phase as confined within closed magnetic loops anchored to the cD galaxy. When combined with so-called Rosner-Tucker-Vaiana mechanism which applies to solar coronae, this model can potentially explain basic properties of the cool phase, including its temperature and thermal stability.

Subject headings: conduction — magnetic fields — plasmas — galaxies: clusters: individual (The Centaurus Cluster) — X-rays:galaxies:clusters

1. INTRODUCTION

Intra-cluster medium (ICM), i.e., the hot plasma confined within the gravitational potential of clusters of galaxies, constitutes the most dominant *known* form of baryons. The ICM was thought to cool over the Hubble time by emitting optically-thin thermal X-rays, because its radiative cooling time is estimated to be $\sim 10^8$ yr at the center of many “cD clusters” (those hosting cD galaxies at their centers). This inspired so-called cooling flow (hereafter CF) hypothesis (e.g. Fabian 1994). The idea was apparently supported by several soft X-ray features observed around cD galaxies, including general decreases of the ICM temperature, strong excess X-ray surface brightness, and excess photoelectric absorption up to a few times 10^{21} cm $^{-2}$.

With the first imaging capability over a broad X-ray energy band up to 10 keV and a much improved energy resolution than was available before, *ASCA* (Tanaka, Inoue & Holt 1994) has provided a number of new results that altogether cast serious doubt upon the reality of CFs. These include; a shortage of the predicted cool gas in the Hydra-A cluster (Ikebe et al. 1997); the presence of uncooled ICM in 3-dimensional core regions of the Centaurus cluster (Fukazawa et al. 1994; Ikebe et al. 1999); a central excess brightness of Abell 1795 that does not depend strongly on the X-ray energy (Xu et al. 1998); hierarchical potential structures in several galaxy groups (Ikebe et al. 1996; Matsushita et al. 1998); and systematic differences in the ICM chemical composition between the central and outer regions of cD clusters (Fukazawa et al. 2000). We compiled all these results in Makishima et al. (2001, hereafter Paper I), and argued that the classical CF hypothesis needs a significant revision. The *ASCA* suggestions have been reconfirmed and reinforced by *Chandra* and *XMM-Newton* (e.g. Tamura et al. 2001a; Kaastra et al. 2001; Peterson et al. 2001).

Although the CF scenario in its original form is no longer considered valid, the ICM temperature of a cD cluster does decrease toward the center. Furthermore, the deprojected radial ICM temperature profiles of a fair number of clusters all reduce to a single “univer-

sal” profile (Allen, Schmidt & Fabian 2001; Kaastra et al. 2004), which reach, at the cluster center, a minimum value of

$$T_c = (1/2 \sim 1/3)T_h \quad (1)$$

(Allen, Schmidt & Fabian 2001; Kaastra et al. 2004). Here, T_h is the ICM temperature observed outside ~ 100 kpc. It is yet to be explained how the intriguing universal temperature profile and the scaling of eq.(1) are produced, and how they are related to mechanisms which suppress CFs.

The concept of the universal temperature profile is based on a “single-phase” (hereafter 1P) picture, that the ICM at a given three-dimensional radius is represented by a single dominant temperature which monotonically decreases toward the center. In contrast, the original *ASCA* results on cD clusters (Paper I) are based primarily on a “two-phase” (hereafter 2P) view; the ICM consists of a “hot phase” and a “cool phase”, intermixed together, with the volume filling factor of the latter increasing toward the center. This view was at the beginning motivated by the complex angular response of the *ASCA* telescopes, but was reinforced *a posteriori* by the fact that 2P fits to the *ASCA* spectra of a cluster generally give a pair of well-defined temperatures regardless of the two-dimensional radii used to extract the signal photons (e.g. Fukazawa et al. 1994; Paper I). In other words, the 2P modeling is likely to be more than a mere convention.

Generally, the hot-phase and cool-phase temperatures, derived under the 2P assumption, are respectively close to T_c and T_h of eq.(1) obtained through the 1P analysis. Furthermore, eq.(1) holds for the 2P results as well (Ikebe 2002). The 1P and 2P approaches are thus consistent in the sense that both yield essentially the same two characteristic temperatures, T_c and T_h . Nevertheless, their physical implications are much different. The 1P situation would require a fine tuning between the radiative cooling and the putative heating mechanism, or “quasi-hydrostatic” gas cooling (Masai & Kitayama 2004). To realize the 2P condition, in contrast, the cool phase must be thermally insulated from the hot phase, and heated in a stable manner, so that it should neither evaporate (Takahara & Takahara 1979), nor collapse due to cooling. Yet another possibility is that the ICM temperature takes a range of values even at a single radius (Kaastra et al. 2004); this is to be called “multi-phase” picture.

In order to identify the CF-suppression mechanism, it is of basic importance to clarify which of the 1P and 2P pictures (or the multiphase view) is closer to the reality. In spite of its importance, there have been few attempts to address this issue. We hence analyze in the present paper the *XMM-Newton* data of the Centaurus cluster. This object is best suited to our purpose, because it harbors the very prominent cool component and has extensively been studied with *ASCA*. Our strategy is to examine whether or not deprojected spectra of this cluster require the presence of multiple temperatures at each 3-dimensional radius. The

data will also allow us to reconfirm the lack of emission with temperature below the value of eq.(1).

In §2, we briefly summarize previous X-ray results on the Centaurus cluster, and describe the *XMM-Newton* observations in §3. Section 4, which forms the core of the present paper, is devoted to the description of data analysis and results. The results are discussed in §5, followed by a summary in §6. Throughout the paper, the Hubble constant is expressed as $H_0 = 72 \text{ km }^{-1} \text{ Mpc}^{-1}$. The three-dimensional radius and the projected radius are denoted as R and r , respectively. Errors represent 90 % confidence limits unless stated otherwise.

2. PREVIOUS X-RAY RESULTS ON THE CENTAURUS CLUSTER

Located at a redshift of $z = 0.0104$ (Lucey, Currie & Dickens 1986; Smith et al. 2000) where $1'$ corresponds to 12.5 kpc, the Centaurus cluster (Abell 3526) is one of the most well studied objects among nearby clusters. It exhibits a roughly round shape, and its cD galaxy, NGC 4696, does not show significant nuclear activity. In X-rays, the Centaurus cluster has been observed extensively, with *Uhuru* (Giacconi et al. 1972; Forman et al. 1978), *OSO8* (Mushotzky et al. 1978), *HEAO1* (Mitchell & Mushotzky 1980), *Einstein* (Matilsky, Jones & Forman 1985), *EXOSAT* (Edge & Stewart 1991a,b), and *Ginga* (Yamashita 1992). These observations yielded an ICM temperature of $\sim 4 \text{ keV}$, except in the central region ($r \lesssim 6'$) where a very prominent cool component and an excess brightness are observed.

Allen & Fabian (1994) studied the Centaurus cluster using the data from the *ROSAT* PSPC. They found some evidence of metallicity increase and excess absorption at the center. Through a deprojection analysis, they also derived 3-dimensional properties of the ICM under the 1P modeling, reporting that the ICM is cooled down to $\sim 1 \text{ keV}$ toward the center.

Using *ASCA* with the much improved energy resolution and the wider energy band, Fukazawa et al. (1994) successfully resolved both the Fe-K line and low-energy emission lines, and detected hot and cool components with a temperature of ~ 4 and $\sim 1 \text{ keV}$, respectively. The strong metallicity increase toward the center was reconfirmed. They also discovered that the 3-dimensional core region ($R < 5'$) of the cluster is filled mostly with the hot component, whereas the cool component occupies a minor fraction of the volume. Through a more detailed analysis of the *ASCA* data, Ikebe (1995) showed that the 1P density and temperature profiles derived with *ROSAT* (Allen & Fabian 1994) underpredict the hard X-ray flux from the central region, and hence fail to explain the 0.5–10 keV *ASCA* data. Ikebe (1995) instead found that the *ASCA* spectra from various regions near the center can be described adequately by the 2P formalism employing the two components

identified by Fukazawa et al. (1994). This reinforced the presence of the hot phase in the three-dimensional core region, and justified the 2P approach.

The 2P formalism on the Centaurus cluster was further refined and reinforced by Ikebe et al. (1999). Incorporating two temperatures of $T_h \sim 4$ keV and $T_c \sim 1.4$ keV, together with a central metallicity increase, they successfully constructed a 3-dimensional ICM model that can simultaneously explain the *ROSAT* surface brightness and the *ASCA* annular spectra, namely the best-quality data sets available at that time. The excess absorption at the center, claimed by Fabian et al. (1994) based on the *ASCA* data, was not reconfirmed by Ikebe et al. (1999).

Utilizing the unprecedented angular resolution of *Chandra*, Sanders & Fabian (2002) detected a “plume” like X-ray feature near the center of the Centaurus cluster, reconfirming a previous observation with the *ROSAT* High Resolution Imager (Sparks, Jedrzejewski & Macchetto 1994). Within $10''$ of the center including the “plume” region, a cool plasma component with a temperature of ~ 0.7 keV was clearly detected (Sanders & Fabian 2002). Employing the 1P formalism, Sanders & Fabian (2002) also derived the ICM temperature distribution near the center ($\sim 3'$), but the field of view of *Chandra* was not wide enough to determine the global temperature structure over the entire “cool” region ($r \lesssim 6'$).

There are some indications that a subcluster centered on the elliptical galaxy NGC 4709 is merging with the main body. This region exhibits an excess X-ray surface brightness and a temperature increase to ~ 5 keV (Churazov et al. 1999; Furusho et al. 2001; Molendi et al. 2002). However, these effects, seen $\sim 15'$ off the center, are considered to be small in regions which we analyze ($r < 12'$). In fact, using *Suzaku*, Ota et al. (2007) showed that the ICM within the central $\sim 12'$ can be regarded as hydrostatic: specifically, they set an upper limit of $\sim 1,400$ km s $^{-1}$ on any large-scale (~ 100 kpc) bulk motion in the ICM over this region, and ruled out a previously claimed detection of significant bulk motions (Dupke & Bregman 2006).

3. OBSERVATIONS AND DATA REDUCTION

3.1. Observation

The Centaurus cluster was observed with *XMM-Newton* on 2002 January 3 for a gross exposure of 45 ksec. The boresight was set to $(\alpha^{2000}, \delta^{2000}) = (12^{\text{h}}48^{\text{m}}49^{\text{s}}.3, -41^{\circ}18'40''.0)$. The EPIC PN and MOS were operated both in the full frame mode with the thin filters (Strüder et al. 2001; Turner et al. 2001), while the RGS in spectroscopy mode (den Herder et al. 2001).

The EPIC dataset obtained in the same observation were already analyzed by Matsushita et al. (2007a) mainly for metallicity distributions. The present paper emphasizes the temperature structure. Similarly, Sanders et al. (2008) utilized the RGS data from the same observation, as well as those from an additional 110 ks observation.

3.2. EPIC Data Reduction

3.2.1. Data processing

The EPIC data were extracted using the standard SAS software of version 5.4.1. We selected events with $pattern \leq 4$ for PN and $pattern \leq 12$ for MOS, with which most of the valid X-ray events are accepted. According to instructions by the detector team, we further discarded events with bad flags, e.g., those out of the field of view and those detected at bad CCD pixels.

Soft protons often cause the EPIC background to increase suddenly by up to two orders of magnitude. These sporadic “flares” must be removed carefully when analyzing extended sources. We accordingly produced 2–7 keV band light curves of the present data, excluding a central region ($r \lesssim 8'$) where the cluster emission dominates. This particular energy band was shown by Katayama et al. (2004) to serve as a good measure of the EPIC background, and is roughly optimized in the present case to provide a high signal-to-ratio for proton flares; below ~ 2 keV the cluster signals become significant, while above ~ 7 keV the fluorescent background lines in the PN spectra become a nuisance. The results are shown in Figure 1. Following Katayama et al. (2004) and Takahashi (2004), we then discarded those time periods when the count rates deviate by more than 2σ from those in quiescent periods. After this screening, the net exposure time became 31 ksec with PN and 43 ksec with MOS.

Several faint point sources are found in the field of view. We excluded regions where their signals are significant, typically within $15''$ of each source.

3.2.2. Background

Since the cluster emission fills nearly the entire EPIC field of view, background spectra must be constructed using some other “blank sky” data. For this purpose, we utilized the observation of PG 1115+080 for PN (ObsId=0082340101), and that of Vik 59 for MOS (ObsId=0107860501), because these data sets showed a close similarity to the present Centaurus data in terms of high-energy (11–14 keV for PN and 10–12 keV for MOS) count rates accu-

mulated over peripheral regions of the fields of view.

After removing proton flares and celestial point X-ray sources in the same manner, we extracted background events from these data sets, using the same regions on the detectors as employed to accumulate the on-source data. The background derived in this way is estimated to be accurate generally to within $\sim 3\%$, except at some particular spectral regions (Katayama et al. 2004), as detailed in §3.2.4, where we employ 8% . This accuracy is sufficient for our purpose, because the cluster emission is much brighter than the background, e.g., by more than a factor of five, at least up to $\sim 5'$ from the aimpoint in energies below 5 keV. Thus, the background uncertainty therein is at most a few percent of the cluster signal.

3.2.3. Deprojection

To discriminate the 1P and 2P conditions, it is essential to remove the projection effects, using so-called deprojection procedure. To create deprojected spectra, we employed the standard “onion peeling” method (e.g. Ikebe, Böhringer & Kitayama 2004), assuming that the object is spherically symmetric, and the plasma is uniformly distributed in each thin shell region. No model spectra were assumed in our deprojection procedure. Specifically, at each energy E , we calculated the deprojected spectrum $S_j(E)$ in the j -th shell as

$$S_j(E) = \sum_{k \geq j}^N \mathcal{D}_{j,k} A_k(E) , \quad (2)$$

where $A_k(E)$ is the projected spectrum accumulated over the k -th annulus, $\{\mathcal{D}_{j,k}\}$ is a triangular matrix derived by inverting the projection matrix, and N denotes the outermost annulus.

Below, we utilize the data within $12'$ (150 kpc) of the X-ray centroid at $(12^{\text{h}}48^{\text{m}}49^{\text{s}}.2, -41^{\circ}18'44'')$, which coincides with the NGC 4696 nucleus. The emission outside $12'$, $S_N(E)$, was calculated assuming that the plasma is isothermal and isoabundance at $R > 10'$, and that the ICM density profile is expressed by a β model determined jointly with *ASCA* and *ROSAT*, namely $\beta = 0.57$ and the core radius of $7'.3$ (Ikebe et al. 1999). These parameters can reproduce the *XMM-Newton* images themselves (Takahashi 2004). Actual matrix elements of $\{\mathcal{D}_{i,j}\}$ are numerically given in Appendix A.

3.2.4. *Systematic Errors*

In order to take into account calibration uncertainties, conservative systematic errors of 2% (Lumb et al. 2002) were assigned to the on-source spectra in energies above 0.6 keV. Below that energy, the systematic error was increased to 5% to represent uncertainties in the quantum efficiency around the oxygen absorption edge (e.g. Katayama et al. 2004).

To further consider systematic uncertainties involved in the background subtraction process, we assigned to the background data the systematic errors as given in Table 1. The errors are thus taken to be 8% (§3.2.2) in those energy bands where the background is dominated by instrumental fluorescence lines, because their intensities are known to vary rather independently of that of the background continuum. In energies below ~ 1 keV, the background spectra are significantly contributed by diffuse soft X-ray background, of which the brightness varies from sky to sky. There, we hence employed the same 8% systematic error, although the background in this energy range is generally negligible compared to the bright cluster emission. In other energy regions, we employed a nominal value of 3% (§3.2.2).

3.3. RGS Data Reduction

Again using the SAS software, we processed the RGS data, and extracted the first and second order spectra within $r = 60''$ (in the cross-dispersion direction) of the center. The spectral range of 6–23 Å was analyzed, in order to utilize many atomic lines therein.

The RGS background was derived from blank sky fields which were made available by the instrument team (Tamura, den Herder & Gonzáres-Riestra 2003). Because these authors reported that the rms fluctuation of the RGS background is not more than 30% over the full spectral range, we assigned a systematic error of 30% to the RGS background. In reality, the emission from the Centaurus cluster exceeds the background by more than an order of magnitude over the interested spectral range; therefore, the background uncertainties have little effects on the results.

4. DATA ANALYSIS AND RESULTS

4.1. EPIC Data Analysis

4.1.1. EPIC Spectra

Figure 2 shows the PN spectra of the Centaurus cluster, obtained by accumulating the on-source events over a series of concentric annular regions centered on the NGC 4696 nucleus (§3.2.1), and then subtracting the background described in §3.2.2. The radii defining these annuli are given in the figure caption. The figure also shows their ratios to those averaged over an outer region of $5' < r < 12'$, where the cool component is hardly seen. The spectra from these regions do not bear strong atomic lines except the Fe-K line at ~ 6.7 keV, and their spectral shapes are very similar to one another. Therefore, these regions at $r \gtrsim 5'$ must be filled with an approximately isothermal hot plasma. The figure also confirms correct background subtraction, because wrong subtraction would make the hardest-band ($\gtrsim 7$ keV) spectra significantly depend on the radius.

Toward the center, in contrast, we can see prominent increases in the line intensities; the Fe-K line enhancement is caused by the metallicity increase, while those of Si-K (at rest-frame energies of 1.86 and 2.01 keV), S-K (2.46 and 2.62 keV), and Fe-L (~ 1 keV) lines are mainly due to the emergence of the cool component.

At the very central region ($r < 1'$), hereafter called “cD region”, Fe-L lines with energies below 1 keV become prominent, indicating the presence of a still cooler plasma with a temperature of $\lesssim 1$ keV. The same inference can be obtained from the drastic increases in the H-like to He-like intensity ratios of the Si-K and S-K lines. We therefore qualitatively reconfirm the *Chandra* detection of the coolest (~ 0.7 keV in temperature) component at the center (Sanders & Fabian 2002).

Applying the procedure described in §3.2.3 to the spectra in Figure 2, we derived de-projected spectra from 11 concentric shells. Some of them are presented in Figure 3, in comparison with the non-deprojected spectra. The deprojection obviously degrades the data statistics, but does not alter the spectral shape very much; the only eye-catching difference is the reduction in the hard X-ray (> 3 keV) flux of the innermost spectra (denoted [cd]), caused by the removal of contributions from the foreground/background hot emission.

4.1.2. *Single-phase analysis*

As first-cut evaluation of the annular spectra of Figure 2, we conducted a conventional single-temperature analysis. This is meant to approximate 1P conditions, but only crudely, because three effects, coupled with the temperature and abundance gradients, would make each spectrum deviate from an exact isothermality; the most dominant one is the projection effects, while the less important ones are the finite angular resolution of the X-ray telescope which mixes up signals from adjacent shells, and the finite thickness of each annulus. Thus, the single-temperature representation should be regarded as a crude approximation here.

We fitted the three projected EPIC spectra from each annulus with a single-temperature APEC model (Smith et al. 2001) with photoelectric absorption, simultaneously but allowing the model normalization to differ among the three detectors. The abundances of O, Ne, Mg, Si, S, Ar, Ca, Fe, and Ni were all left free, while those of C and N were fixed at the solar values by Anders & Grevesse (1989). The redshift was fixed at 0.0104, and the hydrogen column density at the Galactic-line-of-sight value, $8.1 \times 10^{20} \text{ cm}^{-2}$, because Matsushita et al. (2007a) found the absorption to be grossly consistent with it. Since some systematic residuals were observed around the Fe-K line region, we incorporated small gain correction factors, +0.3% to PN, +0.6% to MOS1, and +0.3% to MOS2, all within the reported calibration uncertainties. These improved the fit chi-squared, without significantly affecting the best-fit parameters.

As expected from Figure 2, fits to the cD region spectra left large residuals around the Fe-L energies. We therefore added, in these cases, another cool APEC component with a temperature (left free) of $\sim 0.7 \text{ keV}$, of which the abundances are tied to that of the major component. As a result, the fits were much improved, in agreement with the report by Sanders & Fabian (2002). This modeling should be distinguished from the 2P approach to be examined later.

The 1P model (plus the 0.7 keV component) reproduced the spectra moderately well, although the fits are not necessarily acceptable. Figure 4 (filed circles) shows radial profiles of the obtained parameters. Thus, the plasma temperature approaches a constant value of $\sim 3.8 \text{ keV}$ toward outer regions, while drops inside $5'$, in agreement with the inference from Figure 2b and with the previous results (e.g. Fabian et al. 1994; Fukazawa et al. 1994; Ikebe et al. 1999; Furusho et al. 2001). As mentioned above, the $\sim 0.7 \text{ keV}$ plasma component was needed at $r < 1'$.

In Figure 4, the abundances of Fe and Si are seen to increase toward the center as first revealed with *ASCA* (Fukazawa et al. 1994), while that of oxygen is spatially rather constant. These results are consistent with the single-temperature analysis results from

Matsushita et al. (2007a). Although Sanders & Fabian (2002) reported a *Chandra* detection of a metallicity decrease within $r \sim 45''$ (down to ~ 0.4 solar at $r < 10''$), such an effect, if any, is less significant in the EPIC data.

We performed the same model fitting to the deprojected spectra. Since the spectra are now free from the projection effects, the single-temperature modeling is equivalent to 1P conditions, assuming that each deprojected shell is thin enough and the signal mixing due to the telescope response is negligible. This analysis yielded the data points represented in Figure 4 by open diamonds. Thus, the overall results are very similar to those obtained with the annular spectra. The fits became generally better, due to the reduced statistics of the deprojected spectra, and to the removal of fore- and background contributions. The latter also makes the deprojected temperatures systematically lower (typically by 0.3–0.5 keV) than the non-deprojected values.

4.1.3. Two-phase analysis

As an alternative approach, we fitted the EPIC spectra by a 2P model, i.e., a sum of two APEC components with different temperatures, plus the ~ 0.7 keV component at $< 1'$. For each annulus, the cool component temperature T_c was left free, while the abundance of each element was assumed to be the same among the components. Like in the 1P analysis (§4.1.2), the C and N abundances were fixed; so were the redshift and the photoelectric absorption. When we first let the hot component temperature T_h float as well, it became rather unconstrained in some outer regions, and scattered over a range of ~ 3 to ~ 7 keV. This is due to coupling with T_c (Matsushita et al. 2007a). However, the value was generally consistent, within rather large errors, with 3.8–4.0 keV obtained in past observations. We hence fixed it at $T_h = 3.8$ keV after the *ASCA* results (Ikebe et al. 1999) and our 1P fits (Figure 4).

By this 2P model, both the non-deprojected and deprojected spectra were reproduced reasonably well in all regions. The obtained parameters, shown in Figure 5, are generally consistent with the two-temperature results by Matsushita et al. (2007a) within some differences in the modeling. Thus, the fit goodness is comparable to, or slightly better than, those obtained with the 1P analysis. The derived abundance profiles are essentially the same as the 1P results, and the radial profile of Fe (Fig. 5c) agrees very well with the *ASCA* 2P results (Ikebe et al. 1999). The temperature differences between the projected and non-deprojected spectra became smaller than in the 1P analysis, and often insignificant within errors. This is consistent with a 2P condition, in which an annulus and the corresponding deprojected shell are expected to share nearly the same two temperatures.

Figure 6a shows radial profiles of the emission measures (per unit volume) of the hot and cool components, denoted Q_h and Q_c , respectively. Thus, the cool component is required within $6'$, where the 1P temperature decreases significantly in our 1P result (Figure 4). The derived T_c stays at ~ 2 keV over $2' - 6'$ (though rather poorly determined outside $3'$; Figure 5a), while it decreases down to $T_c \sim 1.6$ keV at the center. The latter agrees with the central 1P temperature from our 1P fits (Figure 4) and from *ROSAT* (Allen & Fabian 1994). At the cD region, the third 0.7 keV component is again required. In contrast, neither the ring-sorted spectra nor the deprojected thin-shell ones required the cool component in regions outside $6'$. Accordingly, Figure 5 outside $6'$ simply reproduces the 1P results.

Incidentally, the 2P analyses of the *ASCA* data yielded somewhat lower values of T_c ; ~ 1 keV (Fukazawa et al. 1994), or 1.4 ± 0.2 keV (Ikebe et al. 1999). This is partially because *ASCA* was not able to separately detect the 0.7 keV component. The remaining difference may be due to the different plasma codes (Matsushita et al. 2007a), the MEKAL and APEC codes used in the *ASCA* study and the present analysis, respectively.

To characterize the obtained 2P solution, let us introduce, after Ikebe et al. (1999), the volume filling factor η_c of the cool phase. Using the emission measures, this quantity is defined as

$$Q_c = \xi n_c^2 \eta_c, \quad Q_h = \xi n_h^2 (1 - \eta_c), \quad (3)$$

where n_h and n_c are the densities of the hot and cool phases, respectively, while ξ is a factor of order unity reflecting the metallicity. Assuming a pressure balance between the two phases (Fukazawa et al. 1994), namely,

$$n_c T_c = n_h T_h, \quad (4)$$

we can calculate η_c as

$$\eta_c = \left[1 + \left(\frac{T_h}{T_c} \right)^2 \left(\frac{Q_h}{Q_c} \right) \right]^{-1}. \quad (5)$$

Figure 6b shows the radial profile of η_c , thus calculated using eq.(5); in deriving this result, we fixed T_c at 2.0 keV in shell regions outside $R = 1'$. The figure reconfirms the *ASCA* results (Fukazawa et al. 1994; Ikebe et al. 1999), that the hot phase dominates the volume down to a radius rather close ($R \sim 1'.5$ or 18 kpc) to the center. The filling factor implied by the *XMM-Newton* data is higher by a factor of ~ 3 than the *ASCA* determination; as can be understood via eq.(5), this is due partially to the higher value of T_c .

4.2. Analysis of Thick-Shell Spectra

As we have seen in §4.1, the two descriptions, 1P and 2P, are consistent with each other in the sense that both find essentially the same set of three plasma temperatures, ~ 3.8 keV, 1.7–2.0 keV, and ~ 0.7 keV. Outside $\sim 6'$ (~ 75 kpc), the ICM can be approximated as isothermal at ~ 3.8 keV. Within $\sim 6'$ toward the cluster core, the ICM becomes gradually cooler down to ~ 2 keV (if employing the 1P description), or the ~ 2 keV plasma becomes intermixed with the hot 3.8 keV component with a progressively larger η_c (if employing the 2P description). In the cD region, both scenarios require the additional 0.7 keV plasma. Up to this stage, we are unable to tell which of the two approaches is more favored by the data. Although the 2P fit to the deprojected spectra often gives a slightly lower reduced chi-squared than the 1P fit (Figure 4b vs. Figure 5b), the difference is not necessarily statistically significant, and could be due to the finite temperature gradient within each shell.

4.2.1. Construction of thick-shell spectra

In order to better distinguish the 1P and 2P modelings under higher statistics, we took the deprojected spectra from consecutive five thin shells covering altogether $R = 1' - 5'$ ([e] though [i] in Figure 2), which have 1P temperatures of 2.03, 2.48, 2.65, 3.10, and 3.30 keV respectively (§4.1.2). We then summed them into a single spectrum which now represents a thicker 3-dimensional shell in the cool core region; this is hereafter called “Shell C”. The cD region, together with the “plume” structure, is excluded to avoid complexity introduced by the 0.7 keV component. Since the statistical errors associated with the adjacent thin-shell spectra are not mutually independent, we estimated the errors to be assigned to the thick-shell spectra by properly considering error propagation utilizing eq.(2)(Takahashi 2004).

The Shell C spectra, one for each detector, should contain the 3.8 keV component if the 2P scenario is correct. If instead the 1P picture is more appropriate, the Shell C spectra would rule out contributions from such a high temperature component, because the 1P temperature changes across Shell C from 2.0 keV to 3.3 keV but not higher (Figure 4). We expect that the improved data statistics, achieved by the spectral summation, allow us to distinguish these two cases.

In addition to the improved statistics, analyzing a thick shell has two more advantages: the signal mixing caused by the finite telescope resolution is reduced, and the errors due to spectral changes within individual thin shells, if any, nearly cancel out. As an instructive exercise of the latter effect, let us assume, for example, the 3rd and 4th annuli constituting Shell C to have a difference by δW in their Fe-K line equivalent widths, and examine what

would happen if we artificially assigned the two annuli with a same value \bar{W} that is the emission-measure-weighted average between the two shells. This exaggerates the procedure of averaging out a radial spectral change over a finite shell thickness. The errors caused by the averaging are expected to propagate through deprojection into the 1st through 4th thin shells. However, as shown in Appendix A, a mathematical estimate using actual matrix elements of eq.(2) confirms that the errors in the four thin shells roughly cancel out, and hence the final thick Shell-C spectrum suffers in the present case no larger errors in the line equivalent width than $\sim 0.01\delta W$. Since the same estimate applies to a temperature gradient, which is at most $\sim 25\%$ in each thin shell (Figure 4) over $1' - 5'$, the residual temperature errors in the Shell C spectrum are estimated to be at most $\sim 0.3\%$, and hence negligible.

4.2.2. *Single-phase modeling*

Let us examine the Shell C spectra against the 1P view. We hence took the best-fit single-temperature APEC model for each of the 5 constituent thin shells, and convolved it with a response of each detector that is weighted by the surface brightness of the projection of the relevant thin shell. In the same way as the actual thick-shell data, we then summed up the 5 simulated thin-shell spectra of each detector into a single one, to be called “synthetic 1P spectrum”.

Figure 7a directly compares these synthetic 1P spectra with the actual Shell C spectra of the corresponding detectors. Thus, we observe a moderately good agreement, but the actual Shell C spectra exhibit some excess above the synthetic 1P model toward higher energies. In fact, their difference, in terms of chi-squared summed over the three detectors (PN, MOS1 and MOS2), becomes $\chi^2/\nu = 739/378$ as summarized in Table 2.

The data vs. model comparison in Figure 7a incorporates no adjustment, since the synthetic 1P spectra are uniquely specified by the best-fit models describing the 5 constituent thin shells (§4.1.2). However, the agreement might be improved by adjusting the model parameters. We therefore allowed to vary freely the normalizations of the five APEC components which constitute the synthetic 1P spectrum. Then, the agreement (now to be called “a fit”) was improved to $\chi^2/\nu = 724/373$ (Table 2); the normalizations of the five components changed by a factor of 1.65, 0.25, 0.84, 1.10, and 1.26 in the increasing order of the temperature, while the summed normalization remained unchanged within $\sim 2\%$. Thus, the coolest and hottest of the five components tend to be enhanced, implying a 2P-like condition. To retain a stable fit convergence, we did not attempt to let the 5 temperatures float.

4.2.3. Two-phase modeling

In order to next examine the 2P approach, we fitted the actual Shell C spectra with a sum of two APEC models, exactly in the same manner as in §4.1.3; the two temperatures and the two normalizations were left free, as were the abundances of O, Ne, Mg, Si, S, Ar, Ca, Fe, and Ni which are assumed to be common to the two components. The relative normalizations among the 3 detectors were left free as before. As a result, the degree of freedom decreased by 15 compared to the synthetic 1P modeling. The two components were convolved with the same response, weighted by the X-ray surface brightness.

As shown in Figure 7b and Table 2, the obtained fit ($\chi^2/\nu = 688/363$) is significantly better than that with the synthetic 1P model, even considering the reduced degree of freedom. In fact, the high energy excess, observed in Figure 7a, has been reduced in Figure 7b. The two temperatures have been obtained as $T_h = 4.02^{+0.41}_{-0.33}$ keV and $T_c = 2.06^{+0.07}_{-0.10}$ keV. While these values agree well with the 2P results from the individual thin shells (Figure 5), the obtained T_h is significantly higher than the temperature range (up to 3.30 keV, with a typical error of ± 0.15 keV) involved in the 1P description of Shell C (Figure 4). Although the error ranges associated with the derived T_h and T_c are somewhat (typically by $\sim 40\%$) underestimated due to rather large values of the reduced chi-squared (~ 1.9), the above inference remains valid even if the error ranges are enlarged by $\sim 40\%$.

Just for consistency, we applied in the same way the 2P fit to the synthetic 1P spectra, to which Poissonian noise was added. This yielded $T_c = 2.3$ keV and $T_h = 3.3$ keV, although the associated errors are rather difficult to estimate. These two temperatures are both contained within the 1P temperature distribution across Shell C (Figure 4), from 2.03 keV to 3.30 keV, that we employed in constructing the synthetic 1P spectra. This difference between the actual Shell C spectrum and the sythetic 1P spectrum suggests that the hot 3.8 keV component was already present in the 5 thin-shell spectra, and has become more significant by the spectral summation.

In the above 2P fit to the actual Shell C spectra, the two components were treated to have the same abundances, and were convolved with the same response. However, the true 2P condition would be somewhat different, since the cool component, more weighted toward the metal-enriched inner regions than the hot one, must have higher abundances when averaged over Shell C. To better express this condition, we returned to the original best-fit 2P models to the five thin-shell spectra, convolved them with projected responses of the respective thin shells, and summed the results over the 5 shells. These simulated data, involving two fixed temperatures (2.0 and 3.8 keV) and properly considering the radial abundance changes, are to be called “synthetic 2P spectra”, because they are constructed exactly in the same way as their 1P counterparts. Although these synthetic 2P spectra do not involve any adjustable

free parameter, they have reproduce the Shell C spectra with $\chi^2/\nu = 678/378$, even better than the above 2P fit, and also than the synthetic 1P modeling.

4.2.4. *Error renormalization*

From the statistical viewpoint, even the synthetic 2P simulation obtained in § 4.2.3 does not give an acceptable reproduction of the data (Table 2). This hampers correct error evaluations, and makes it difficult to quantitatively compare different modelings. In Figure 7, fit residuals are observed around strong emission lines, such as Si-K, S-K, and Ar-K. Therefore, the inadequate fit goodness is likely to be caused mainly by subtle calibration inaccuracy in reproducing the detailed line profiles, rather than model inappropriateness. Under the higher data statistics, the calibration uncertainties presumably exceeded the systematic errors of 2% already assigned in §3.2.4. Although our data analysis utilized rather old SAS version (5.4.1), a reanalysis of a few representative spectra from the central region, using an updated version 7.0.0 SAS software (processing and responses), showed rather insignificant improvements of these problems. Furthermore, the fitting results derived with the two versions agreed within errors. Accordingly, we retain the version 5.4.1 analysis, and assigned 5% of the source counts as a new systematic errors to the whole energy range, and repeated the overall analyses. This procedure is meant to make the fit acceptable when using the model that is best preferred by the data, and to make securer the distinction among different models.

By this error renormalization, the values of χ^2 have reduced appreciably, while the radial profiles of various plasma parameters remained unchanged. Specifically, the comparison of the Shell C spectra with the remade synthetic spectra gives $\chi^2 = 418$ and 381 for 1P and 2P, respectively, both with $\nu = 378$ (Table 2). The latter is statistically acceptable, and gives a chi-squared which is smaller by 30 than the former. Thus, the 2P modeling of the Shell C spectra is statistically superior to the 1P one.

4.2.5. *Thick Shell P spectra*

In a similar way, we derived EPIC spectra from another thick shell, called Shell P, which sums up three consecutive thin shells covering $R = 3' - 6'$. This Shell P is peripheral to the central cool region. The summed Shell P spectra were then compared with the corresponding synthetic 1P and 2P spectra, constructed in the same manner as before from the best-fit solutions to the 3 constituent thin shells. The comparison of the actual spectra with the

synthetic 1P and 2P spectra gave $\chi^2 = 511$ and 496 (without the error renormalization), respectively, both with $\nu = 378$. The difference in chi-squared, though smaller than in the Shell C case, amounts to 15, and remains ~ 11 even when the systematic error is renormalized as in §4.2.4.

We also fitted the Shell P spectra with the 2P model, in the same way as for the Shell C case but fixing T_h at 3.8 keV as we did in §4.1.3. We then obtained $T_c = 2.10^{+0.38}_{-0.29}$ keV, together with $\chi^2/\nu = 494/364$. This value of T_c again agrees with those obtained by the 2P fits to the constituent thin-shell spectra (Figure 5), while it is significantly below the distribution of the 1P temperature across Shell P, 3.0–3.5 keV (Figure 4). Therefore, the cool (~ 2.0 keV) component is inferred to be present even in this relatively outer region. As a consistency check, we fitted the synthetic 1P spectra in Shell P with the same 2P model, and obtained $T_c = 3.2$ keV which agrees with the input 1P temperature range.

4.2.6. Possible artifacts

We have so far found that the two sets of thick-shell spectra both prefer the 2P view to the 1P scenario. However, the results could be subject to various artifacts.

An immediate suspect is that the appearance of the hot component in Shell C is an artifact caused by insufficient background subtraction. However, this would not explain the presence of the cool component in Shell P. Furthermore, the constant spectral shape in $r > 5'$ (§4.1.1; Figure 2) argues against this possibility. For a more quantitative examination, we remade the deprojected spectra with the background artificially under-subtracted, by 3% which is comparable to the background systematic errors estimated in §3.2. In fact, this little affected the results obtained so far: a comparison of the remade Shell C spectra with the 2P synthetic spectra (§4.2.3) gives nearly the same χ^2 as before, changing only by ~ 2 . Thus, our results are robust against the background uncertainty.

Another concern is possible deviations from the so-far assumed spherically symmetry. Indeed, the ICM temperature of the Centaurus cluster exhibits significant non-axisymmetric distributions (Furusho et al. 2001; Molendi et al. 2002; Sanders & Fabian 2002; Fabian et al. 2005). Then, even if the ICM were in a 1T condition, Shell C would sample a wider range of temperatures, to mimic a 2T condition. However, as far as we consider an annular region of $4' < r < 8'$ that is crucial to this issue, the ICM temperature (approximated as 1T) is azimuthally constant typically within $\pm 15\%$ (Furusho et al. 2001). To examine this issue using the present data, we derived a temperature map, presented in Figure 8, by analyzing the projected EPIC spectra in four sectors by a single-temperature model.

It reconfirms a mild temperature decrease from northwest to southeast directions, with an amplitude comparable to those measured previously. According to a simple estimation, a temperature variation of this amount is insufficient, by at least a factor of two, to explain the difference between the two values of $T_h = 4.02^{+0.41}_{-0.33}$ keV and $T_h = 3.03$ keV, obtained via the 2T fit to the Shell C spectrum and its synthetic 1T data, respectively. Thus, the preference for the 2T view remains intact.

The finite angular resolution of the *XMM-Newton* X-ray telescope could also blur the Shell C boundary, and cause contaminations by signals from the outer hotter region. However, Shell C is much thicker ($4'$) than the blurring width ($\sim 15''$), and the surface brightness decreases outwards. As a result, the contamination of the outer hotter emission into Shell C is estimated to be at most $\sim 2\%$, which is within the renormalized systematic uncertainty of 5% introduced in § 4.2.4.

In the deprojection process (§ 3.2.3), we assumed the region outside $12'$ (150 kpc) to have a constant spectrum that is identical to that measured just inside it. This is based on the fact that the azimuthally-averaged ICM temperature of this cluster, measured with the *ASCA* GIS utilizing its wide field of view and low background, is essentially constant at ~ 3.9 keV from $r = 14'$ up to $r = 40'$ (0.5 Mpc; Ikebe et al. 1999). Of course, deviations from this assumption would in principle affect, via eq.(2), the deprojected spectrum in every shell. However, our numerical estimate in Appendix A indicates that the emission from the $R > 12'$ region contributes only $\sim 1\%$ to the Shell C spectrum, and hence any realistic error associated to it is considered negligible. Furthermore, the ICM temperature has been confirmed in many clusters to decrease beyond ~ 0.2 times the virial radius (e.g., Markevitch 1996; De Grandi & Molendi 2002; Sato et al. 2007b; Leccardi & Molendi 2008), or $r \gtrsim 0.5$ Mpc in the present case. Then, we are likely to be overestimating the outermost ICM temperature, and hence over-subtracting the hot (3.8 keV) emission as foreground and background contributions. This makes our argument simply more conservative.

A more difficult issue is asymmetry along the line of sight. If the object has a prolate shape in the depth direction, the deprojected shell C spectra would sample effectively outer (hence hotter) regions, and would involve the 3.8 keV component even if it is in a 1P condition. Similarly, an oblate 1P condition would make Shell P sample the cool emission. However, neither case can explain the two thick shells simultaneously.

Finally in § 4.2.1, possible spectral changes within each thin shell was already shown to become negligible through the construction of thick shells. As an overall confirmation to address this issue, in Appendix B we have numerically simulated a 1P cluster, and analyzed the fake data in the same manner as for the actual data. Then, the simulated Shell C spectra have been reproduced by the 1P view, without demanding the 2P formalism. As a logical

contraposition, the preference of the 2P modeling by the actual data demands the actual object not to be in the 1P condition.

From these examinations, we conclude that the data favor the presence of the hot ~ 3.8 keV component in the 3-dimensional core region ($R = 1' - 5'$), and the cool ~ 2 keV component in the peripheral region ($R = 3' - 6'$). In other word, the 2P picture is considered to describes the actual physical state better than the 1P view.

4.3. Excess Absorption

At the center of the Centaurus cluster, some previous works reported the presence of excess X-ray absorption, up to a few times $\sim 10^{21} \text{ cm}^{-1}$ (depending on the modeling), above the Galactic column (Allen & Fabian 1994; Fabian et al. 1994; Sanders & Fabian 2002); this was taken as evidence for the CF. However, the effect was not confirmed in other works (Ikebe et al. 1999). Likewise, we have here experienced no problems in our spectral analysis with the absorption fixed at the Galactic value.

Generally, a somewhat higher absorption is often derived when a two- (or multi-) temperature emission is fitted with a 1P model (e.g., Matsushita et al. 2007a). However, some of the previously reported excess column densities in the Centaurus cluster considerably exceed such modeling uncertainties.

We examined this issue using the non-deprojected and deprojected spectra from regions within $10''$ and $30''$ of the center, respectively. Specifically, we refitted these EPIC data using the 2P plus 0.7 keV model, applying an intrinsic absorption factor to both components in addition to that due to the Galactic column. (The hot component can be neglect here.) As a result, the fits were little improved in either case. The obtained *excess* column density in the rest frame is $3.2_{-1.8}^{+2.0} \times 10^{20} \text{ cm}^{-2}$ for the non-deprojected spectra within $10''$, and $0.5_{-0.5}^{+2.3} \times 10^{20} \text{ cm}^{-2}$ for the deprojected spectra within $30''$. These are significantly lower than the previously claimed values, $\gtrsim 1 \times 10^{21} \text{ cm}^{-2}$, and the case of the deprojected spectrum is consistent with no excess absorption. Then, what is responsible for this discrepancy?

Regardless of the modeling (1P or 2P), the *XMM-Newton* data reveal that oxygen in the central region is deficient relative to iron and silicon (§4.1.2, §4.1.3). Nevertheless, the previous works usually assumed metals in the ICM to obey the solar abundance ratios, simply because of inadequate energy resolution. This presumably caused data deficits around the oxygen line (~ 0.65 keV) relative to the model predictions, and forced previous investigators to introduce an artificial excess absorption in an attempt to suppress the over-predicted O-K line flux in their models. Actually, if we constrain the ICM to follow the solar abundance

ratios, the present data clearly require an excess absorption by $\sim 1.4 \times 10^{21} \text{ cm}^{-2}$, although the fit becomes worse (with $\chi^2/\nu = 1.38$) compared to the case of the Galactic absorption and free abundance ratios ($\chi^2/\nu = 1.13$). Thus, the reported excess absorption in the Centaurus cluster is considered an artifact, caused mainly by the non-solar abundance ratios around the cD galaxy.

4.4. RGS Results

Because the surface brightness of the Centaurus cluster is strongly peaked at the center, we can utilize the RGS data to better constrain the temperature structure of the ICM in the cD region, although the available spatial information is limited to 1-dimensional projections. We extracted the first and second order spectra from RGS1 and RGS2, over a strip of $2'$ in width centered on the NGC 4696 nucleus. The cross-dispersion direction is at a position angle of $\sim 20^\circ$, so that the data accumulation strip partially covers the plume. The background was subtracted as described in §3.3.

Figure 9a shows the obtained RGS spectrum, which combines the 1st and 2nd order spectra from the two RGS units. Although the energy resolution is somewhat degraded due to the finite angular extent of the source, we clearly observe many atomic emission lines. In particular, the spectrum bears a strong K-line at $\sim 19 \text{ \AA}$ from H-like oxygen ions (OVIII), but lacks those from He-like ones (OVII) which would be emitted strongly at about 22 \AA by plasmas with a temperature lower than 0.3 keV . This indicates that the cluster core region is devoid of such very cool plasmas, contrary to the prediction by the CF hypothesis.

Since we already know that at least two plasma temperatures (0.7 keV and $1.7\text{--}2.0 \text{ keV}$) are required to reproduce the emission from the cD region, we fitted the RGS spectra with a simple 2P plasma emission model; we hereafter call this particular modeling “quasi-2P fit”, because it indeed invokes two APEC components but the employed temperatures are different from those composing the 2P model employed in §4.1.3 and §4.2. The four spectra (1st- and 2nd-order spectra from RGS1 and RGS2) were prepared separately, and fitted jointly. We neglected for the moment the hot (3.8 keV) component, because its high temperature and large angular extent make low-energy lines rather weak, and hence its parameters are difficult to constrain with the RGS data. The abundances of O, Ne, Mg, Si, Fe, and Ni were left free, but constrained to be common between the two components. After the EPIC results (Takahashi 2004), we fixed the S, Ar, and Ca abundances at 1.7, 1.5, and 2.4 solar, respectively, because K-lines of these elements are outside the RGS wavelength range. The absorption is assumed to be Galactic, as confirmed in §4.3. To deal with the spatial extent, we blurred each spectral component with a Gaussian of a free width σ .

The quasi-2P fit to the RGS spectra is shown in panels (b) and (c) of Figure 9, and the obtained parameters are summarized in Table 3. Thus, the overall emission-line features have been reproduced to a reasonable extent. Although the fit is not yet fully acceptable, this is mainly due to some unessential factors, such as our simple spectral blurring, the projection effects, and calibration uncertainties.

The obtained two temperatures, 0.8 keV and 1.7 keV, agree well with the lowest two characteristic values measured with the EPIC from the cD region. The Gaussian widths of the 0.8 keV and 1.7 keV components, $\sim 20''$ and $\sim 65''$ respectively, can be understood as reflecting the angular extent of the ~ 0.7 keV and ~ 1.7 keV component detected with the EPIC. The RGS-determined abundances of Mg, Si, and Fe are lower by a factor of ~ 2 than the values obtained with the EPIC data. The discrepancy is at least partially relaxed by considering the hot (3.8 keV) component, which does not emit prominent lines, but is estimated to contribute to the continuum up to 30% and reduce equivalent widths of the lines by that amount. The remaining abundance discrepancy could be due to the abundance drop at the very center (Sanders & Fabian 2002). In any case, the temperatures, determined primarily by the line intensity ratios, are not affected.

The RGS spectra may be examined for the presence of other temperature components, besides the ~ 0.8 keV and 1.7 keV ones constituting the quasi-2P fit. The RGS spectra were therefore analyzed with the multi-temperature fit procedure of Tamura et al. (2003), which is a kind of differential emission measure analysis like those in Peterson et al. (2003) and Kaastra et al. (2004). Specifically, we prepared seven plasma emission components of which the temperatures are given as T_0 , $1.5T_0$, $(1.5)^2T_0$, ..., and $(1.5)^6T_0$, with T_0 being the lowest temperature. We then allowed to vary the normalizations of the seven components, as well as T_0 to which the remaining 6 temperatures scale. The abundances of O, Ne, Mg, Si, Fe, and Ni were left free, but constrained to be common among the seven components. Each spectral component was blurred with a Gaussian, of which the width is left free but constrained to be less than $66''$ as obtained in the previous fit (Table 3).

As shown in Figure 10, the best fit model obtained from this analysis is physically very close to that obtained with the quasi-2P model. The fit has been improved little ($\chi^2/\nu = 976/718$; cf. Table 3) by considering extra temperature components, with only the two components (~ 0.8 keV and 1.7 keV) remaining significant. Note that these two temperatures are constrained to have a ratio of $1.5^2 = 2.25$, while their absolute values are left free. The 1.1 keV component has turned out to be weak in contrast to the two adjacent ones, implying that the significantly detected two components are discrete entities rather than representing a continuous temperature distribution. The 2.55 keV component is not significant, either.

The RGS results constrain the 3.8 ($=1.7 \times 1.5^2$) keV component to have an emission measure which is $< 30\%$ of that of the 1.7 keV component. Employing eq.(5), the volume filling factor of this component is then estimated as $< [1 + (1.7/3.8)^2/0.3]^{-1} = 0.6$ (or equivalently $\eta_c > 0.4$). This is consistent with Figure 6.

Figure 10 also reconfirms that any cool emission below 0.7 keV is insignificant. The upper limits are by more than an order of magnitude below the prediction of the isobaric CF model (Johnstone et al. 1992), if the model normalization is adjusted to the data at 1.7 keV. Therefore, we conclude that the ICM around NGC 4696 is not cooling to temperatures much below ~ 0.7 keV. Analyzing the RGS data from the present and an additional 110 ks observation, Sanders et al. (2008) also confirmed that the emission measure from the central region decreases more steeply toward lower temperatures than in a simple CF picture.

5. DISCUSSION

5.1. Summary of the Obtained Results

We analyzed the *XMM-Newton* EPIC data of the central region ($< 12'$ or < 150 kpc) of the Centaurus cluster, assuming a spherical symmetry. The ICM has been characterized by three representative temperatures; $T_h \sim 3.8$ keV, $T_c = 1.7 - 2.0$ found within $\sim 6'$ (75 kpc), and ~ 0.7 keV localized within $\sim 1'$ (12 kpc) of the center. The values of T_c and T_h are consistent with the *ASCA* measurements (Ikebe et al. 1999), and satisfy eq.(1). Similarly, the detection of the 0.7 keV component reconfirms the *Chandra* result (Sanders & Fabian 2002). The RGS data from the core region reinforced the presence of these discrete temperatures, and gave tight upper limits to emission with a temperature of < 0.5 keV.

5.1.1. $2T$ vs. $1T$ preference

As far as the deprojected thin-shell spectra are individually analyzed, the data had no preference between the 1P and 2P approaches. However, the two sets of EPIC spectra from 3-dimensional thicker shells have revealed that the hot component is present even in a very inner ($R < 5'$) region, and the cool component protrudes out beyond $R \sim 3'$ (§4.2). The RGS results from the cD region (§ 4.4) provides an important support to this view. Takahashi (2004) found that *XMM-Newton* spectra of the central regions of Abell 1795 also prefer the 2P formalism to the 1P modeling.

In principle, the ICM could be in multi-temperature conditions (Kaastra et al. 2004).

Since a spectrum resulting from such a superposition of a range of temperatures is rather insensitive to the way of superposing them (Craig & Brown 1976), an apparently 2P plasma may well be in a multi-temperature condition, and vice versa, particularly when the energy resolution is not too high. Indeed, the measured value of T_c appears to distribute from 1.7 to 2.0 keV, depending on the radius. Nevertheless, the RGS data preferred the presence of discrete temperatures, to a continuous temperature distribution (§4.4). Therefore, a multi-phase modeling of the ICM is considered inappropriate, at least the cD region of the Centaurus cluster is concerned.

Based on these results, we suggest that the plasmas in the central ~ 75 kpc of the Centaurus cluster are better envisaged by invoking a few (two to three) discrete temperature components, rather than assuming a continuous radial temperature gradient or a condition of differential emission measure. These results support and extend our view of cD clusters developed with *ASCA* (Paper I). Below, we adopt the 2P view as our working hypothesis.

When integrated up to $R = 12'$ (150 kpc), the hot component, the cool component, and the 0.7 keV one have bolometric luminosities of $L_h^{\text{bol}} = 3 \times 10^{43} \text{ erg s}^{-1}$, $L_c^{\text{bol}} = 1.0 \times 10^{43} \text{ erg s}^{-1}$, and $L_{0.7}^{\text{bol}} = 6 \times 10^{41} \text{ erg s}^{-1}$, respectively. According to Ikebe et al. (1999), L_h^{bol} increases by a factor of 2 if integrated further out to $R = 30'$ (375 kpc).

5.1.2. ICM abundances

We have determined the radial abundance profiles of Fe, Si and O in the ICM, assuming that the different plasma components share the same abundances at a given radius. Those of the other elements are much more uncertain (Takahashi 2004). As first discovered by Fukazawa et al. (1994), and already reported by Matsushita et al. (2007a) by analyzing the present *XMM-Newton* data, the Fe and Si abundances have been reconfirmed to increase significantly toward the center (Figure 5), and stay rather high even at the very center. The Si/Fe abundance ratio at the center, about 1.3 (Figure 5), agrees with the *ASCA* measurements (Fukazawa et al. 2000).

In contrast to the behavior of Fe and Si, the O abundance is radially more constant, implying a decrease in the O/Fe ratio toward the center, in agreement with Matsushita et al. (2007a). As argued by various authors (Paper I; Mushotzky et al. 1996; Fukazawa et al. 1998, 2000; Sato et al. 2007a; Kawaharada 2006; Kawaharada et al. 2009), this can naturally be understood as a result of varying contributions from type Ia and type II supernovae: the outer-region ICM is contributed significantly by oxygen-rich products from type II supernovae, while that in the inner region by iron-rich products from type Ia supernovae that

occurred in the cD galaxy.

So far, a fair number of other clusters have been known to exhibit abundance profiles similar to those of the Centaurus cluster, with a central increase of iron and silicon, and a flat distribution of oxygen (e.g. Böhringer et al. 2001; Tamura et al. 2001b; Kawaharada et al. 2009). These include in particular recent *Suzaku* observations of the Fornax cluster (Matsushita et al. 2007b), Abell 1060 (Sato et al. 2007b), and AWM 7 (Sato et al. 2008). Therefore, the relative oxygen deficit in the cluster core region may be a common phenomenon.

5.1.3. Evidence against Cooling Flows

The present results argue against the CF scenario from several independent aspects. These include; the lack of cooling component (§4.4); the lack of excess absorption (§4.3); and the radial changes in the abundance ratios (§5.1.2) which rule out large-scale inflows of the ICM. Below, we discuss the first two issues in some more details.

The CF scenario relates the bolometric luminosity, L_{CF} , of a “cooling” portion of ICM with the mass deposition rate, \dot{M} , as (Fabian 1994)

$$L_{\text{CF}} = \frac{5\dot{M}kT_{\text{h}}}{2\mu m_{\text{p}}}, \quad (6)$$

where μ is the mean molecular weight and m_{p} is the proton mass. By substituting the measured value of $L_{\text{c}}^{\text{bol}} + L_{0.7}^{\text{bol}} = 1.1 \times 10^{43} \text{ erg s}^{-1}$ (§5.1) into L_{CF} , we obtain $\dot{M} = 11 M_{\odot} \text{ yr}^{-1}$. This in itself is consistent with the previous results from *ROSAT* (Edge, Stewart & Fabian 1992; Peres et al. 1998) and *ASCA* (Paper I). However, we have found no evidence of emission from any plasma component with a temperature $< 0.5 \text{ keV}$, with upper limits much tighter than the CF-predicted emission measure (Figure 10). Therefore, the CF interpretation fails to explain the strong cool emission of the Centaurus cluster, as well as in other clusters (Paper I; Tamura et al. 2001a; Kaastra et al. 2001; Peterson et al. 2001). The value of \dot{M} should not be taken as an actual mass-deposition rate.

We have shown in §4.3 that the previously reported excess absorption, at the center of the Centaurus cluster, is an artifact caused by the relative oxygen deficit. In fact, when the non-solar abundance ratios are properly considered, the absorption became consistent with being Galactic only, with any additional column at most several times 10^{20} cm^{-2} . As discussed in §5.1.2, the relative oxygen depletion in the cluster center appears to be a common feature. Then, the excess absorption, claimed previously in many other clusters (e.g. White et al. 1991), will be explained away as well. Indeed, using the RGS spectra,

Peterson et al. (2003) also confirmed the lack of excess absorption from several other clusters. Given these results, there is practically no evidence for the X-ray absorbing materials at least in nearby well-studied clusters.

5.2. The 0.7 keV component

Let us briefly consider the nature of the 0.7 keV component, which is localized to the cD galaxy, NGC 4696. Similar cool emission components are seen around other cD galaxies, including M87 in particular, but their interpretation has generally been unsettled (e.g., Fabian et al. 2001a; Churazov et al. 2001; Molendi 2002).

Judging from the angular extent (~ 20 kpc) and the bolometric luminosity (6×10^{41} erg s^{-1}), this 0.7 keV component could be hot interstellar medium (ISM) associated with the cD galaxy. Its temperature is consistent with the stellar velocity dispersion of NGC 4696, 274 km s^{-1} . The plasma emitting this component (including both the central concentration and the plume) has an estimated mass of a few times $10^9 M_{\odot}$ (Sanders & Fabian 2002), which is also consistent with this ISM interpretation. Although the estimated cooling time of this plasma is as short as $\sim 10^8$ yr (Sanders & Fabian 2002), the radiative energy loss could be supported by such processes in NGC 4696 as the supernova heating (a few times 10^{41} erg s^{-1}), and the accumulation of stellar mass loss which is dynamically “hot” on the galaxy scale.

In contrast to the above arguments, the complex filamentary morphology of this component (Sanders & Fabian 2002), including the plume like elongated tail structure, cannot easily be reconciled with the hot ISM interpretation, even considering interactions of the cD galaxy with the ICM. Similar problems with the cool gas in M87 (the Virgo cD galaxy) were pointed out by Molendi (2002), who showed its close association with the synchrotron radio arms. Furthermore, as exploited in Paper I, the hot ISM interpretation could be applied better to the cool (2 keV) component. Considering these, the 0.7 keV plasma could alternatively be associated with some magnetic structures around the cD galaxy, which in turn could be a result of past nuclear activity in NGC 4696. Further discussion of this issue is beyond the scope of the present paper.

5.3. A Magnetosphere Model

The successful 2P picture (§4.2, §5.1.1) and the absence of significant CFs (§5.1.3) in the Centaurus cluster suggest that its core region (within ~ 75 kpc) hosts a cool plasma phase

which is stably intermixed with the hot phase. While this reconfirms a prediction made in Paper I, it poses a series of questions to be answered; (i) how such a 2P configuration is realized; (ii) how the cool phase is heated against the radiative cooling; (iii) how the heating and cooling be balanced in a thermally stable manner; (iv) what determines the value of T_c ; and (v) what produces the scaling of eq.(1). Below, we examine them one by one.

5.3.1. Needs for ordered magnetic fields

An immediate issue associated with the 2P scenario is (i) how to realize such a configuration. We may suppose that the two phases are intermixed on a typical length scale of $a \sim 10$ kpc, as indicated by various sharp structures seen in X-ray images of some clusters (Fabian et al. 2001b; Machacek et al. 2005; Iizuka 2006), including the “cold front” structure (Vikhlinin et al. 2001). Then, employing the classical Spitzer heat conductivity,

$$\kappa = 5 \times 10^{-7} T^{5/2} \text{ ergs s}^{-1} \text{ cm}^{-1} \text{ K}^{-1} \quad (7)$$

where T is the temperature in Kelvin, the time scale of conductive heat exchange between the two phases would be very short, as

$$\tau_{\text{cond}} \sim 6 \times 10^5 \left(\frac{n_e}{10^{-3} \text{ cm}^{-3}} \right) \left(\frac{T_h}{4 \text{ keV}} \right)^{-5/2} \left(\frac{a}{10 \text{ kpc}} \right)^2 \text{ yr} \quad (8)$$

(Sarazin 1988). The two phases would quickly become isothermal, unless the heat conduction between them is suppressed (Takahara & Takahara 1979; Asai, Fukuda & Matsumoto 2006).

The most natural way to suppress the heat conduction is to invoke magnetic fields, as argued, e.g., by Molendi (2002) to explain the cool plasma in M87. In fact, the ICM is known to be generally magnetized to a few μG , and the aforementioned sharp X-ray features themselves are indicative of ordered strong ($\sim 10 \mu\text{G}$) magnetic fields (Vikhlinin et al. 2001). In the particular case of the Centaurus cluster, a magnetic field strength up to $\sim 25 \mu\text{G}$ is reported from radio observations (Taylor et al. 2007). Although these field strengths are not necessarily higher than the equipartition value ($\sim 30 \mu\text{G}$), they are more than sufficient to completely suppress the heat transport across field lines, because the gyration radius of 4 keV thermal electrons in a $1 \mu\text{G}$ field, $\sim 10^8$ cm, is more than 10 orders of magnitude smaller than their classical mean free path for Coulomb scattering which also determines eq.(7). In contrast, the heat conductivity along field lines may well be approximated by the Spitzer value, eq.(7), unless the field lines are highly tangled (Malyshkin & Kulsrud 2001).

Based on solar analogy, magnetic field lines around a cD galaxy may be classified grossly into “open” and “closed” ones (Makishima 1997), corresponding to coronal holes and coronae, respectively. This view relies only on a general and simple classification of the magnetic field-line topology, without invoking any particular magnetic configuration. Then, open-field regions, connected to the outer cluster volume, must be filled with the hot-phase ICM, and kept nearly isothermal by the efficient field-aligned heat conduction of eq.(7). In contrast, closed-field domains, connected to the cD galaxy and thermally insulated from the surrounding hot phase, can take independent (possibly lower) temperatures of its own. In addition, the loop interior plasma is expected to be metal enriched by type Ia supernovae in the cD galaxy.

From these considerations, we speculate that the plasma, filling numerous magnetic loops anchored to the cD galaxy, is observed as the cool phase of the Centaurus cluster (and of other similar objects). In other words, the cool phase may be regarded as a “magnetosphere” associated with the cD galaxy (Paper I; Makishima 1997). The magnetic fields, while working as a thermal insulator between the two phases, need not to be as strong as the equipartition value, since the loop-interior plasma is confined primarily by external pressure from the hot phase. This “magnetosphere” picture was already invoked successfully in Paper I to explain the *ASCA* results.

Indeed, $H\alpha$ -emitting filamentary features are optically observed in central regions of some clusters on a spatial scale of a few to few tens kpc (e.g., Conselice et al. 2001), and the brightest of them can even be identified in some *Chandra* X-ray images (e.g. Fabian et al. 2003). The best example is the recent *Chandra* result on M87 (Forman et al. 2007), which reveals rich filamentary structures with a typical length of 10 to 50 kpc. In the Centaurus cluster as well, regions of strong magnetic fields are reported to be associated with filamentary structures that emit $H\alpha$ photons and enhanced soft X-rays (Taylor et al. 2007). While these filaments could be limb-brightened edges of bubbles blown by the active galactic nucleus of M87 (Forman et al. 2007), they can alternatively trace magnetic structures such as assumed there.

In addition to these X-ray and radio results, magnetohydrodynamic numerical simulations by Asai, Fukuda & Matsumoto (2007), including both the radiative cooling and the field-aligned heat conduction, show the emergence of low-temperature regions along the loop-shaped magnetic field lines. From these arguments, we believe we have found a viable answer to the issue (i) raised at the beginning of the present section.

5.3.2. *The Rosner-Tucker-Viana mechanism*

We may assume that the cluster core region is fed with a constant heating luminosity H , via some mechanism to be specified later in §5.4. In such a case, the volume heating rate will be generally proportional to the local ICM density, while the volume emissivity is obviously proportional to the density squared. Therefore, denser regions would preferentially cool and become even denser, leading to a thermal instability: this is the issue (iii). If, however, adopting the magnetosphere picture, the cool phase can be thermally stabilized by a built-in feedback mechanism, hereafter called RTV mechanism, originally developed by Rosner, Tucker & Vaiana (1978) to explain quiet solar coronae.

The RTV mechanism holds for a thin magnetic flux tube hydrostatically immersed in an external pressure, with the two loop footpoints anchored to a cool matter reservoir. The loop-interior plasma is assumed to be heated with a constant luminosity H , either uniformly along the loop or at the loop summit. The deposited heat H is assumed to flow toward the footpoints due to loop-aligned conduction of eq.(7), and ultimately radiated away from various heights of the loop. Suppose that H was initially balanced by the radiative cooling, but some perturbation caused H to decrease. Then, the loop loses its internal pressure, and becomes thinner under the external compression, thus reducing the conductive heat flow along it. At the same time, some portion of the plasma flows into the matter reservoir, and the consequent decrease in the emission integral reduces the radiative energy loss. These concordant effects bring the loop into a new steady state corresponding to a lower value of H . Thus, the RTV mechanism thermally stabilizes the cool phase, and gives an answer to the issue (iii).

Following the original work by Rosner, Tucker & Vaiana (1978), Kano & Tsuneta (1995, 1996) used the *Yohkoh* spacecraft to examine the RTV mechanism. They confirmed that it is likely to be actually working in quiescent solar coronae, which keep emitting X-rays in an apparently steady manner for a time much longer than the nominal cooling time (~ 30 minutes).

5.3.3. *Cool-phase temperature*

The RTV mechanism further allows us to answer (iv), namely, to explain the absolute values of T_c . Let us assume that the matter reservoir at the footpoints is much cooler than the loop interior, so that heat inflow to the reservoir can be neglected. Under such boundary conditions, the temperature of the loop-confined plasma is shown to take the maximum value

of

$$T_{\max} = (1.1 - 1.4) \times 10^3 (p_{\text{ext}} l)^{1/3} \quad (\text{K}) \quad (9)$$

at the loop top (Rosner, Tucker & Vaiana 1978; Kano & Tsuneta 1995). Here, l (cm) is the loop half length, and p_{ext} is the loop-confining external pressure in units of dyn cm^{-2} . This is so-called RTV temperature scaling, which is actually confirmed in quiescent solar coronae (Kano & Tsuneta 1995, 1996). The range of the coefficient, 1.1 to 1.4, reflects differences in the assumed heat input distribution along the loop. The index of scaling in eq.(9) depends weakly on the form of the cooling function (Kano & Tsuneta 1996); the particular value of $1/3$ is valid over a temperature range of 0.5–2 keV and near-solar abundances.

Most importantly, T_{\max} in eq.(9) is determined solely by the product $p_{\text{ext}} l$, without depending on H . The loop-interior density n_e becomes also independent of H , because $p_{\text{ext}} \propto n_e T_{\max}$ is assumed to be constant. Changes in H affect only the loop cross section S , and hence the cool-phase X-ray luminosity which is by definition equal to H . More specifically, eq.(7) and eq.(9), together with $H \propto \kappa T_{\max} S/l$, can be combined into another scaling relation as

$$S \propto H p_{\text{ext}}^{-7/6} l^{-1/6} . \quad (10)$$

Thus, the loop becomes thicker under higher values of H . The loop also gets thicker if we decrease p_{ext} while keeping H constant, but in this case, T_{\max} automatically decreases via eq.(9), so as to reduce the conductive heat flux (per unit cross section) $\propto \kappa T_{\max}/l$ and hence keep H unchanged.

In the present case of Centaurus, we may identify p_{ext} with the hot-phase pressure in the core region, namely $p_h = 2n_h k T_h \sim 1 \times 10^{-10} \text{ dyn cm}^{-2}$ with $n_h \sim 1 \times 10^{-2} \text{ cm}^{-3}$ (Ikebe et al. 1999), and rewrite eq.(9) as

$$T_{\max} = (2.0 - 2.5) \left[\left(\frac{p_h}{1 \times 10^{-10}} \right) \left(\frac{l}{30 \text{ kpc}} \right) \right]^{1/3} \text{ keV} . \quad (11)$$

Here, we assumed that loop semi-length to be comparable to the narrower core radius, $\sim 30 \text{ kpc}$, of the double- β modeling for the gravitational potential in the Centaurus cluster (Ikebe et al. 1999). This is because each magnetic loop, with its interior having a higher density than the surrounding hot phase, may not become taller than the flat core radius of the central gravitational potential. The assumed length is comparable to those of the soft X-ray filaments in M87 (Forman et al. 2007).

When such a loop is observed as an integrated entity, we expect to measure an X-ray temperature averaged over the loop length. Assuming the footpoint temperature to be 0.7 keV (§5.2), a simple numerical solution to the RTV equation predicts this average to be

$\sim 0.7 T_{\text{max}}$, or $1.4 - 1.8$ keV from eq.(11). This is in an excellent agreement with T_c actually measured in the Centaurus cluster, giving an answer to the issue (iv).

In reality, the loop length may well scatter, with longer loops tending to be hotter according to eq.(11). Then, we expect the spherically averaged loop temperature to slightly increase outward, because each loop is hottest at its top region, and a larger radii would sample longer loops. This agrees with what we actually observe in Figure 5.

5.3.4. *The T_c vs. T_c scaling*

Taking it for granted that T_c can be identified with $\sim 0.7 T_{\text{max}}$, let us consider the issue (iv), namely, to explain the scaling of eq.(1). The luminosity of the hot phase in a cluster is empirically known to scale with its temperature as $L_h \propto T_h^{3.0}$ (e.g., White, Jones & Forman 1997). On the other hand, we generally have $L_h \propto n_h^2 R_h^3 T_h^{1/2}$, where R_h is a typical radius of the hot phase. Elimination of L_h from these two equations gives $n_h \propto T_h^{5/4} R_h^{-3/2}$, and hence $p_h \propto n_h T_h \propto T_h^{9/4} R_h^{-3/2}$. Substituting this into eq.(11), we obtain

$$T_c \propto T_h^{3/4} R_h^{-1/2} l_h^{1/3} . \quad (12)$$

Assuming that $R_h^{-1/2} l_h^{1/3}$ is relatively constant, T_c indeed becomes roughly proportional to T_h , providing an explanation to eq.(1).

As shown so far, the RTV mechanism can account for the stable coexistence of the cool and hot phases in the cluster core region. The scenario is independent of the amount of available heat input, because a lower value of H simply reduces the cool-phase luminosity. Furthermore, the RTV scaling can quantitatively explain the absolute values of T_c , as well as its (near) proportionality to T_h expressed by eq.(1). Thus, three of the four issues raised at the beginning of §5.3 have been answered. We therefore propose the magnetosphere model, incorporating the RTV mechanism, as a promising hypothesis to explain the plasma physics in the central regions of cD clusters in general.

5.3.5. *Galaxy vs. ICM interaction*

To complete our new viewpoint, we may ask ourselves why the bright cool emission is observed predominantly around cD (or XD) galaxies (Jones & Forman 1984, Figure 1 of Paper I), including NGC 4649. Conversely, non-cD galaxies, like NGC 4472 in the Virgo cluster, generally lack such bright cool X-ray emission, even if they are optically as luminous as their cD counterparts.

An outstanding characteristic of a cD galaxy is that it is nearly in a standstill at the bottom of the gravitational potential. Then, we may speculate that a substantial magnetosphere can develop around a galaxy in a cluster environment only when it is at rest with respect to the ICM. When a galaxy is moving through the ICM, its magnetosphere will be disrupted by the ICM ram pressure, which can be one to two orders of magnitude higher than the magnetic pressure of the assumed magnetosphere (Paper I). Such strong interactions are actually revealed by *Chandra* observations in nearby clusters (e.g., Machacek et al. 2005; Iizuka 2006). Furthermore, optical observations of distant clusters reveal numerous blue spiral galaxies with distorted morphology (e.g., van Dokkum & Franx 2001), which we suggest to be interacting with the ICM.

5.4. Possible Heating Mechanisms

Having answered four out of the 5 questions raised at the beginning of §5.3, the only remaining issue is (ii), i.e., to seek for possible heating mechanisms to sustain the cool-phase luminosity. In the case of the Centaurus cluster, the target value is $H = L_c^{\text{bol}} = 1.0 \times 10^{43} \text{ erg s}^{-1}$. After Makishima (1997), Paper I, and the discussion conducted so far, we retain our magnetosphere viewpoint.

The argument in §5.3.5 indicates that moving galaxies in a cluster interact with the ICM, and transfer their kinetic energies to the ICM. This process is estimated to proceed at a rate of

$$L_{\text{int}} \sim N n m_p v^3 \pi R_{\text{int}}^2 \quad (13)$$

(Sarazin 1988), where N is the number of moving galaxies, n is the average ICM number density, v is the average galaxy velocity, and R_{int} is the interaction radius for each galaxy. We may use $v = 1,010 \text{ km s}^{-1}$ which is $\sqrt{3}$ times the velocity dispersion of the Centaurus cluster (586 km s^{-1}) after Lucey, Currie & Dickens (1986), $n \sim 0.8 \times 10^{-3} \text{ cm}^{-3}$ which is an average over the central 300 kpc (Ikebe et al. 1999), and $N \sim 50$. Furthermore, a relatively large value of R_{int} , say, $\sim 5 \text{ kpc}$, is suggested by the argument in §5.3.5, and by some X-ray observations (Iizuka 2006). Through eq.(13), these numbers yield $L_{\text{int}} \sim 4.5 \times 10^{43} \text{ erg s}^{-1}$, which well exceeds $L_c^{\text{bol}} \sim 1 \times 10^{43} \text{ erg s}^{-1}$. Therefore, the galaxy-ICM interaction becomes a promising candidate for the ICM heating, and for the suppression of CFs. These effects have been reproduced successfully by numerical simulations (Asai, Fukuda & Matsumoto 2007).

How large is the kinetic energy E_{kin} stored in the moving galaxies? The stellar mass of the Centaurus cluster within the central 300 kpc, but excluding the cD galaxy, is estimated as $1.5 \times 10^{12} M_{\odot}$ (Ikebe et al. 1999) after correcting for the different values of the Hubble constant. We have then $E_{\text{kin}} \sim 1.5 \times 10^{61} \text{ ergs}$, which is likely to be a lower limit because

the employed galaxy mass assumes a conservative mass-to-light ratio of 8. As a result, the time scale of the energy transfer from the moving galaxies to the ICM is estimated as $E_{\text{kin}}/L_{\text{int}} \sim 1.1 \times 10^{10}$ yr. Therefore, the kinetic energy in the moving galaxies is large enough to sustain L_{int} over the Hubble time.

The galaxy-to-ICM energy transfer is expected to cause galaxies to gradually fall to the potential center. There are several pieces of observational evidence suggesting that this effect is actually taking place. In fact, the stellar-mass distributions in many clusters are known to be much more centrally peaked than that of the ICM. Furthermore, clear central decreases in “iron-mass to light ratio”, observed from a fair number of clusters and groups (Paper I; Kawaharada 2006; Kawaharada et al. 2009), suggest that galaxies used to be distributed more widely than today, and polluted the ICM with metals out to the cluster edges.

The energy released by the moving galaxies may be stored once in the ICM in the form of turbulence and bulk flows. However, according to the *Suzaku* observation (Ota et al. 2007), these kinetic energies in the ICM of the Centaurus cluster, as estimated from the width and position-dependent centroid shifts of the Fe-K line, cannot largely exceed its thermal energy. Therefore, the turbulent and bulk-flow energies must be dissipated and thermalized efficiently in the ICM, with a rate comparable to L_{int} . If a fair fraction of the dissipated energy is deposited onto the magnetosphere, the available heating luminosity of the cool phase becomes of the order of $H \sim 1 \times 10^{43}$ erg s $^{-1}$ which can just sustain the observed $L_{\text{c}}^{\text{bol}}$. We would rather say that $L_{\text{c}}^{\text{bol}}$ is self-adjusted, via the RTV mechanism, to match the predetermined energy dissipation rate. The remaining portion of L_{int} will heat the hot phase, to make it spatially more extended than the total gravitating mass.

The actual dissipation of turbulence and bulk-flow energies may take place through magnetohydrodynamic processes. For example, moving galaxies will pick up magnetic field lines in the ICM and stretch them, exciting Alfvén waves and causing field lines to reconnect. When the magnetic reconnection occurs between two closed magnetic loops, the released energy will be spent in heating the cool phase. That between closed and open field lines will expel a small portion of the metal-rich cool-phase plasma into the hot phase. The ejected plasmoid will become quickly isothermal with the hot phase, in terms of the electron temperature via eq.(7), as well as in terms of the ion ionization temperature (in a few times 10^7 yr; Masai 1984). The resulting highly ionized heavy ions will remain there due to their slow diffusion (Ezawa et al. 1997), and increase the metallicity of the hot phase. This can explain why the central metallicity increase is observed in both phases.

In addition to the above mechanism, there can be another ICM heating mechanism localized around each cD galaxy; namely, a shrink of its self-gravitating core. Since this has already been discussed in Paper I, we simply mention that this mechanism can also account

for a heating luminosity of $\sim 1 \times 10^{43}$ erg s $^{-1}$.

6. CONCLUSION

Analyzing the *XMM-Newton* EPIC and RGS data of the Centaurus cluster, we have obtained the following results.

1. The ICM in the central ~ 75 kpc can be described better by the two-phase view (plus the 0.7 keV component at < 12 kpc) than by the single-phase picture.
2. There is no evidence of cooling flows.
3. The iron and silicon abundances increases significantly in the central region, while that of oxygen is radially constant.
4. The previously reported excess X-ray absorption disappears when the central oxygen deficit is considered.
5. The overall results agree with those by Ikebe et al. (1999) who used *ASCA* and *ROSAT*.

To explain these observations, we have developed a working hypothesis (after Paper I), in which the cool phase is thought to constitute a magnetosphere associated with the cD galaxy. Incorporating the Rosner-Tucker-Vaiana mechanism, it can account for the following essential features of the Centaurus cluster, as well as of similar cD clusters.

1. The hot and cool ICM phases co-exist in the cluster core region.
2. The ICM is provided with a heating luminosity, which is high enough to sustain the X-ray emission against the radiative cooling.
3. The cool phase is kept thermally stable.
4. The cool phase has a typical temperature of ~ 2 keV, with a mild outward increase.
5. A good proportionality holds between the cool and hot temperatures.
6. The ICM metallicity becomes enhanced in both phases toward the center.

The present results thus provide a new insight into the physics of clusters of galaxies.

Acknowledgements: This work was supported in part by Grant-in-Aid for Scientific research (S) (Japanese Ministry of Education, Culture, Sports, Science & Technology) #18104004 on “Study of Interactions between Galaxies and Intra-Cluster Plasmas”, as well as by Special Research Project for Basic Science (Institute of Physical and Chemical Research) on “Investigation of Spontaneously Evolving Systems”.

Appendix A: The Deprojection Matirx

This Appendix is meant to provide numerical details of the deprojection process described in §3.2.3. Let us consider 11 annular regions, of which the outer radii are at $0'.5$, $1'.0$, $1'.5$, $2'$, $3'$, $4'$, $5'$, $6'$, $8'$, $10'$, and $12'$, and the corresponding 11 shell regions. These divisions are the same as used in Figures 2, 4, and 5, except that the innermost 4 regions therein are here re-arranged into two regions just for clearer presentation. The reconstructed “Shell C” spectrum, namely $C \equiv \sum_{j=3}^7 S_j$, is not affected by this simplified treatment of inner annuli/shells. Let $(A_1, A_2, \dots, A_{11})$ be the projected spectra from the 11 annular regions at a given energy, while $(S_1, S_2, \dots, S_{11})$ those from the 11 shells. Note A_{11} has the outer boundary at $12'$, while S_{11} includes emission outside that. Then, let $\mathcal{M}_{i,j}$ denote the projection matrix which converts $\{S_i\}$ into $\{A_j\}$. In the present geometrical setting, it is numerically given as

$$\begin{pmatrix} A_1 \\ A_2 \\ A_3 \\ A_4 \\ A_5 \\ A_6 \\ A_7 \\ A_8 \\ A_9 \\ A_{10} \\ A_{11} \end{pmatrix} = \begin{pmatrix} 1.000 & 0.258 & 0.083 & 0.041 & 0.020 & 0.010 & 0.006 & 0.004 & 0.003 & 0.002 & 0.004 \\ 0 & 0.742 & 0.329 & 0.137 & 0.063 & 0.031 & 0.019 & 0.013 & 0.008 & 0.005 & 0.011 \\ 0 & 0 & 0.588 & 0.321 & 0.116 & 0.055 & 0.032 & 0.021 & 0.013 & 0.008 & 0.018 \\ 0 & 0 & 0 & 0.501 & 0.213 & 0.083 & 0.047 & 0.031 & 0.018 & 0.011 & 0.026 \\ 0 & 0 & 0 & 0 & 0.588 & 0.321 & 0.151 & 0.093 & 0.055 & 0.032 & 0.074 \\ 0 & 0 & 0 & 0 & 0 & 0.501 & 0.303 & 0.152 & 0.083 & 0.047 & 0.105 \\ 0 & 0 & 0 & 0 & 0 & 0 & 0.443 & 0.285 & 0.122 & 0.064 & 0.137 \\ 0 & 0 & 0 & 0 & 0 & 0 & 0 & 0.401 & 0.199 & 0.086 & 0.174 \\ 0 & 0 & 0 & 0 & 0 & 0 & 0 & 0 & 0.501 & 0.303 & 0.477 \\ 0 & 0 & 0 & 0 & 0 & 0 & 0 & 0 & 0 & 0.443 & 0.724 \\ 0 & 0 & 0 & 0 & 0 & 0 & 0 & 0 & 0 & 0 & 1.113 \end{pmatrix} \begin{pmatrix} S_1 \\ S_2 \\ S_3 \\ S_4 \\ S_5 \\ S_6 \\ S_7 \\ S_8 \\ S_9 \\ S_{10} \\ S_{11} \end{pmatrix} \quad (14)$$

On the assumption that the emission is uniform within each individual shell, these matrix elements are uniquely determined by the geometry alone, without any dependence on the emission model or instrumental effects. The only exception is the last column, namely $\mathcal{M}_{i,11}$ ($i = 1, 2, \dots, 11$), which assumes the emission outside $12'$ as explained in §3.2.3. Although the matrix elements are shown with only 3 digits below decimal points, this is again for simplicity; the calculation is preformed with double precision.

By inverting this matrix, we can calculate the deprojection matrix $\{\mathcal{D}_{i,j}\}$ defined in eq.(2). Numerically, it is calculated as

$$\begin{pmatrix} S_1 \\ S_2 \\ S_3 \\ S_4 \\ S_5 \\ S_6 \\ S_7 \\ S_8 \\ S_9 \\ S_{10} \\ S_{11} \end{pmatrix} = \begin{pmatrix} 1.00 & -0.347 & 0.054 & -0.022 & 0.000 & -0.001 & -0.000 & -0.000 & -0.000 & -0.000 & 0.000 \\ 0 & 1.347 & -0.753 & 0.113 & -0.035 & 0.002 & -0.004 & -0.001 & -0.001 & -0.000 & -0.000 \\ 0 & 0 & 1.700 & -1.089 & 0.058 & -0.042 & 0.001 & -0.005 & -0.002 & -0.001 & -0.001 \\ 0 & 0 & 0 & 1.998 & -0.722 & 0.132 & -0.057 & 0.006 & -0.005 & -0.001 & -0.002 \\ 0 & 0 & 0 & 0 & 1.700 & -1.089 & 0.167 & -0.101 & -0.006 & -0.009 & -0.007 \\ 0 & 0 & 0 & 0 & 0 & 1.998 & -1.367 & 0.215 & -0.083 & 0.002 & -0.019 \\ 0 & 0 & 0 & 0 & 0 & 0 & 2.259 & -1.608 & 0.090 & -0.076 & -0.017 \\ 0 & 0 & 0 & 0 & 0 & 0 & 0 & 2.494 & -0.992 & 0.192 & -0.090 \\ 0 & 0 & 0 & 0 & 0 & 0 & 0 & 0 & 1.998 & -1.367 & 0.034 \\ 0 & 0 & 0 & 0 & 0 & 0 & 0 & 0 & 0 & 2.259 & -1.471 \\ 0 & 0 & 0 & 0 & 0 & 0 & 0 & 0 & 0 & 0 & 0.899 \end{pmatrix} \begin{pmatrix} A_1 \\ A_2 \\ A_3 \\ A_4 \\ A_5 \\ A_6 \\ A_7 \\ A_8 \\ A_9 \\ A_{10} \\ A_{11} \end{pmatrix} \quad (15)$$

From eq.(15), the Shell C spectrum C at each energy can be expressed as

$$C = (1.700A_3 + 0.909A_4 + 1.036A_5 + 0.999A_6 + 1.003A_7) - (1.493A_8 + 0.005A_9 + 0.085A_{10} + 0.045A_{11}). \quad (16)$$

Thus, the outermost annulus A_{11} , which is most subject to the background uncertainty as well as to that of the emission outside $R = 12'$, contributes *geometrically* only less than 5% to the Shell C spectrum, compared to the individual shells A_3 through A_7 . In addition, the flux in A_{11} is ~ 3 to ~ 30 times lower than those in the 3rd to 7th annuli (Figure 2). Considering these, we estimate that the emission from the $R > 12'$ region contributes *physically* by no more than $\sim 1\%$ to the Shell C spectrum. Therefore, any systematic error associated with A_{11} is concluded to be negligible (§4.2.6).

Another exercise to be conducted using eq.(15) is the issue raised in § 4.2.1, i.e., how the assumption of emission constancy within each thin shell affects our Shell C spectrum. As mentionned there, let us examine what happens if we purposely neglected spectral differences between A_5 and A_6 (the 3rd and 4th thin shell constructing Shell C, respectively), where the 1P properties change rather steeply with R . Taking the Fe-K line equivalent width as an example, we may write the fluxes in the Fe-K line energy region as $A_5 = B_5(1 + W_5)$ and $A_6 = B_6(1 + W_6)$, where B represents continuum and W the line equivalent width. Using the difference $\delta W \equiv W_5 - W_6$ and the emission-measure-weighted mean $\bar{W} \equiv (B_5W_5 + B_6W_6)/(B_5 + B_6)$, we may rewrite as $A_5 = B_5 [1 + \bar{W} + B_6\delta W/(B_5 + B_6)]$ and $A_6 = B_6 [1 + \bar{W} - B_5\delta W/(B_5 + B_6)]$. Substitution of this into eq.(16) readily yields

$$C = C' + (1.036B_5 + 0.999B_6)(1 + \bar{W}) + 0.037\alpha (B_5 + B_6)\delta W \quad (17)$$

where C' represents terms unrelated to A_5 or A_6 , while $\alpha \equiv B_5B_6/(B_5 + B_6)^2 \leq 1/4$ is a numerical factor. Thus, the negligence of δW between the two annular spectra has only an effect of at most $\sim 0.01\delta W$ in the Shell C spectrum. The essence is that the deprojection procedure has mathematically “differential” nature exaggerating small-scale features, while this problem is largely removed by constructing a thick shell wherein a process of integration is involved. This is evidenced by eq.(16), where C is close to a simple summation of A_3 through A_7 , except that A_3 must be given a 1.7 times larger weight and A_8 (the shell just outside Shell C) must be subtracted with a relatively large weight of 1.5.

Appendix B: A Numerical Simulation of an 1P Cluster

In order to assess the validity of our “thick shell” method, the following numerical simulation was performed. We started from the best-fit 1P numerical models (Figure 4)

obtained for the 13 deprojected thin shell regions which are defined in Figure 2. Then, to represent the radial spectral changes more smoothly, each of the 5 shells constituting Shell C (covering $r = 1' - 5'$) was subdivided into inner and outer halves, and appropriate temperature and emission measure were assigned to the inner/outer pair. These model spectra, now comprising 18 shells, were projected numerically onto the corresponding 18 annuli, to form numerical spectral models for the 18 annular regions. At this stage, the inner/outer pair were numerically recombined together. The derived 13 model spectra were convolved with the EPIC energy responses, and were given Poisson errors simulating the actual observation. Then, in the same manner as the actual data, we analyzed these 13 annular spectra via deprojection.

Figure 11 shows the simulated Shell C spectra, compared with the “synthetic 1P spectra” introduced in §4.2.2. The comparison is fully satisfactory with $\chi^2/\nu = 324.96/322 = 1.009$. For reference, a 2P fit with two APEC components, in the same manner as explained in §4.2.3, gave $\chi^2/\nu = 312.9/309 = 1.013$, which is similarly acceptable. In other words, the 1P and 2P interpretations degenerate unlike the case of the actual data. Furthermore, unlike the 2P fit to the actual Shell C spectra which revealed the $T_h \sim 4$ keV component, the 2P fit to the simulated data yielded $T_c = 2.00^{+0.14}_{-0.35}$ keV and $T_h = 3.11^{+0.09}_{-0.16}$ keV, which are both consistent with the assumed 1P temperature range (2.03 to 3.30 keV).

REFERENCES

- Allen, S. W. & Fabian, A. C. 1994, MNRAS, 269, 409
- Allen, S. W., Schmidt, R. W. & Fabian, A. C. 2001, MNRAS, 328, L37
- Anders, E. & Grevesse, N. 1989, Geochim. Cosmochim. Acta, 53, 197
- Asai, N., Fukuda, N. & Matsumoto, R. 2006, Astron. Nachr. 327, 605
- Asai, N., Fukuda, N. & Matsumoto, R. 2007, in Heating versus Cooling in Galaxies and Clusters of Galaxies, Eso Astrophysics Symposia(Springer-Verlag Berlin Heidelberg), 2007, p. 228
- Böhringer, H. et al. 2001, A&A, 365, L181
- Churazov, E., Brüggen, M., Kaiser, C. R., Böhringer, H., & Forman, W. 2001, ApJ, 554, 261
- Churazov, E., Gilfanov, M., Forman, W. & Jones, C. 1999, ApJ, 520, 105, 1999
- Conselice, C. J., Gallagher, J. S. III & Wyse, R. F. G. 2001, Astron. J., 122, 2281
- Craig, I. J. D., & Brown, J. C. 1976, Nature, 264, 340
- De Grandi, A., & Molendi, S. 2002, ApJ, 567, 163

- den Herder, J. W. et al. 2001, *A&A*, 365, L7
- Dupke, R. A. & Bregman, J. N. 2006, *ApJ*, 639, 781
- Edge, A. C. & Stewart, G. C. 1991a, *MNRAS*, 252, 414
- Edge, A. C. & Stewart, G. C. 1991b, *MNRAS*, 252, 428
- Edge, A. C., Stewart, G. C. & Fabian, A. C. 1992, *MNRAS*, 258, 177
- Ezawa, H., Fukazawa, Y., Makishima, K., Ohashi, T., Takahara, F., Xu, H. & Yamasaki, N. Y. 1997, *ApJ*, 490, L33
- Fabian, A. C. 1994, *ARA&A*, 32, 277
- Fabian, A. C., Arnaud, K. A., Bautz, M. W. & Tawara, Y. 1994, *ApJ*, 436, L63
- Fabian, A. C., Mushotzky, R. F., Nulsen P. E., & Peterson, J. R. 2001a, *MNRAS*, 321, L20
- Fabian, A. C., Sanders, J. S., Crawford, C. S., Conselice, C. J., Gallagher, J. S., & Wyse, R. F. G. 2003, *MNRAS*, 344, L48
- Fabian, A. C., Sanders, J. S., Taylor, G. B. & Allen, S. W. 2005, *MNRAS*, 360, L20
- Fabian, A. C., et al. 2001b, *MNRAS*, 321, L33
- Forman, W., Jones, C., Cominsky, L., Julien, P., Murray, S., Peters, G., Tananbaum, H. & Giacconi, R. 1978, *ApJS*, 38, 357
- Forman, W. et al. 2007, *ApJ*, 665, 1057
- Fukazawa, Y., Ohashi, T., Fabian, A. C., Canizares, C. R., Ikebe, Y., Makishima, K., Mushotzky, R. F. & Yamashita, K. 1994, *PASJ*, 46, L55
- Fukazawa, Y., Makishima, K., Tamura, T., Nakazawa, K., Ezawa, H., Ikebe, Y., Kikuchi, K. & Ohashi, T. 2000, *MNRAS*, 313, 21
- Fukazawa, Y., et al. 1998, *PASJ*, 50, 185
- Furusho, T., Yamasaki, N. Y., Ohashi, T. S. R., Kagei, T., Ishisaki, Y., Kikuchi, K., Ezawa, H. & Ikebe, Y. 2001, *PASJ*, 53, 421
- Giacconi, R., Murray, S., Gursky, H., Kellogg, E., Schreier, E., Tananbaum, H. 1972, *ApJ*, 178, 281
- Iizuka, R. 2006, Ph.D thesis, University of Tokyo
- Ikebe, Y. 1995, Ph.D. thesis, University of Tokyo
- Ikebe, Y. 2002, in *ASP Conf. Ser. 268, Tracing Cosmic Evolution with Galaxy Clusters*, ed. S. Borgani, M. Mezzetti & R. Valdarnini (San Francisco; ASP), 169 (astro-ph/0112132)
- Ikebe, Y., Böhringer, H. & Kitayama, T. 2004, *ApJ*, 611, 175
- Ikebe, Y. et al. 1996, *Nature*, 379, 427
- Ikebe, Y. et al. 1997, *ApJ*, 481, 660

- Ikebe, Y., Makishima, K., Fukazawa, Y., Tamura, T., Xu, H., Ohashi, T. & Matsushita, K. 1999, *ApJ*, 525, 58
- Johnstone, R. M., Fabian, A. C., Edge, A. C. & Thomas, P. A. 1992, *MNRAS*, 255, 431
- Jones C. & Forman, W. 1984, *ApJ*, 276, 38
- Kaastra, J. S., Ferrigno, C., Tamura, T., Paerels, F. B. S., Peterson, J. R. & Mittaz, J. P. D. 2001, *A&A*, 365, L99
- Kaastra, J. S. et al. 2004, *A&A*, 413, 415
- Kano, R. & Tsuneta, S. 1995, *ApJ*, 454, 934
- Kano, R. & Tsuneta, S. 1996, *PASJ*, 48, 535
- Katayama, H., Takahashi, I., Ikebe, Y., Matsushita, K. & Freyberg, M. J. 2004, *A&A*, 414, 767
- Kawaharada, M. 2006, Ph.D. thesis, University of Tokyo
- Kawaharada, M., Makishima, M., Kitaguchi, T., Okuyama, S., Nakazawa, K., Matsushita, K. Fukazawa, Y. 2009, *ApJ*, 691, 971
- Leccardi, A., & Molendi, S. 2008, *A&A*, 486, 359
- Lucey, J. R., Currie, M. J. & Dickens, R. J. 1986, *MNRAS*, 221, 453
- Lumb, D. H., Warwick, R. S., Page, M. & De Luca, A. 2002, *A&A*, 389, 93
- Machacek, M., Dosaj, A., Firman, W., Jones, C., Markevitch, M., Vikhlinin, A., Warmflash, A. & Kraft, R. 2005, *ApJ*, 621, 663
- Makishima K. 1997, in *Imaging and Spectroscopy of Cosmic Hot Plasmas*, ed. F. Makino, K. Mitsuda (Universal Academy Press, Tokyo) p137
- Makishima, K. et al. 2001, *PASJ*, 53, 401
- Malyshev, L. & Kulsrud, R. 2001, *ApJ*, 549, 402
- Markevitch, M. 1996, *ApJ*, 465, L1
- Masai, K. 1984, *Ap&SS*, 98, 367
- Masai, K. & Kitayama, T. 2004, *A&A*, 421, 815
- Matilsky, T., Jones, C. & Forman, W. 1985, *ApJ*, 291, 621
- Matsushita, K., Makishima, K., Ikebe, Y., Rokutanda, E., Yamasaki, N. & Ohashi, T. 1998, *ApJ*, 499, L13
- Matsushita, K., Böhringer, H., Takahashi, I & Ikebe, Y. 2007a, *A&A*, 462, 953
- Matsushita, K., et al. 2007b, *PASJ*, 59, S327
- Mitchell, R. & Mushotzky, R. 1980, *ApJ*, 236, 730
- Molendi, S., De Grandi, S., & Guainazzi, M. 2002, *A&A*, 392, 13
- Molendi, S. 20020, *ApJ*, 580, 815

- Mushotzky, R. F., Serlemitsos, P. J., Boldt, E. A., Holt, S. S. & Smith, B. W. 1978, ApJ, 225, 21
- Mushotzky, R. F., Loewenstein, M., Arnaud, K. A., Tamura, T., Fukazawa, Y., Matsushita, K., Kikuchi, K. & Hatsukade, I. 1996, ApJ, 466, 686
- Ota, N. et al. 2007, PASJ, 59, S351
- Peres, C. B., Fabian, A. C., Edge, A. C., Allen, S. W., Johnstone, R. M. & White, D. A. 1998, MNRAS, 298, 416
- Peterson, J. R. et al. 2001, A&A, 365, L104
- Peterson, J. R. et al. 2003, ApJ, 590, 207
- Rosner, R., Tucker, W. D. & Vaiana, G. S. 1978, ApJ, 220, 643
- Sanders, J. S. & Fabian, A. C. 2002, MNRAS, 331, 273
- Sanders, J. S., Fabian, A. C., Allen, S. W., Morris, R. G., Graham, J. & Johnstone, M. 2008, MNRAS, 385, 1186
- Sato, K., Matsushita, K., Ishisaki, Y., Yamasaki, N. Y., Ishida, N. & Ohashi, T. 2007a, ApJ, 667, L41
- Sato, K. et al. 2007b, PASJ, 59, 299
- Sato, K. et al. 2008, PASJ, 60, S333
- Sarazin, C. J., *X-ray emission from clusters of galaxies*, Cambridge University Press, 1988
- Smith, R. J., Lucey, J. R., Hudson, M. J., Schlegel, D. J. & Davies, R. L. 2000, MNRAS, 313, 469
- Smith, R. K., Brickhouse, N. S., Liedahl, D. A. & Raymond, J. C. 2001, ApJ, 556, L91
- Sparks, W. B., Jedrzejewski, R. I. & Macchetto, F. 1994, in AIP Conf. Proc. 313, The Soft X-ray Cosmos, ed. E. M. Schlegel & R. Peter (New York; AIP), 389
- Strüder, L. et al. 2001, A&A, 365, L18
- Takahara, F. & Takahara, M. 1979, Prog. Theor. Phys. 62, 1253
- Takahashi, I. 2004, Ph.D. thesis, University of Tokyo
- Tamura, T. et al. 2001a, A&A, 365, L87
- Tamura, T., Bleeker, J. A. M., Kaastra, J. S., Ferringno, C. & Molendi, S. 2001b, A&A, 379, 107
- Tamura, T., Kaastra, J. S., Makishima, K. & Takahashi, I. 2003, A&A, 399, 497
- Tamura, T., den Herder, J. W. & Gonzáres-Riestra, R. 2003, RGS Background Files, XMM-SOC-CAL-TN-0034 issue 1.0, ESA
- Tanaka, Y., Inoue, H. & Holt, S. S. 1994, PASJ, 46, L37
- Taylor, G. G., Fabian, A. C., Gentile, G., Allne, S. W., Crawford, C., & Sanders, J. S. 2007, MNRAS, 382, 67

- Turner, M. J. L. et al. 2001, *A&A*, 365, L27
- van Dokkum P. G., & Franx M. 2001, *ApJ*, 553, 90
- Vikhlinin, A., Markevitch, M. & Murray, S. S. 2001, *ApJ* 549, L47
- White, D. A., Fabian, A. C., Johnstone, R. M., Mushotzky, R. F. & Arnaud, K. A. 1991, *MNRAS*, 252, 72
- White, D. A., Jones, C. & Forman, W., *MNRAS*, 292, 419
- Xu, H., Makishima, K., Fukazawa, Y., Ikebe, Y., Kikuchi, K., Ohashi, T. & Tamura, T. 1998, *ApJ*, 500, 738
- Yamashita, K. 1992, in *Proceedings of the Yamada Conference XXVIII, Frontiers of X-Ray Astronomy*, ed. Y. Tanaka and K. Koyama (Tokyo; University Academy Press), 475

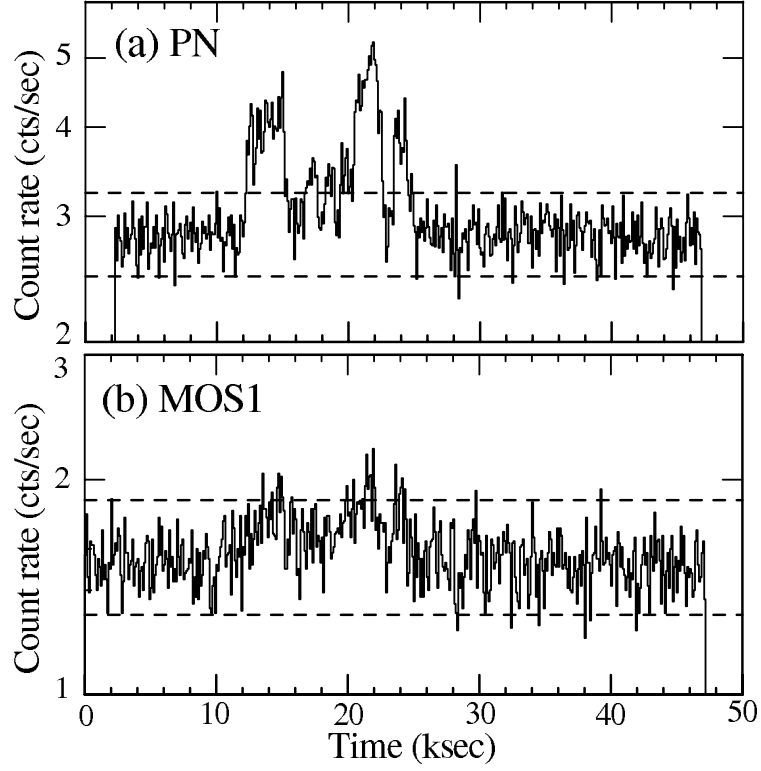


Fig. 1.— EPIC PN (panel a) and MOS1 (panel b) light curves in 2–7 keV from the present observation, obtained by excluding the central ($r < 8'$) region. The bin width is 100 sec. The dashed lines indicate $\pm 2\sigma$ levels from the mean values in the quiescent periods.

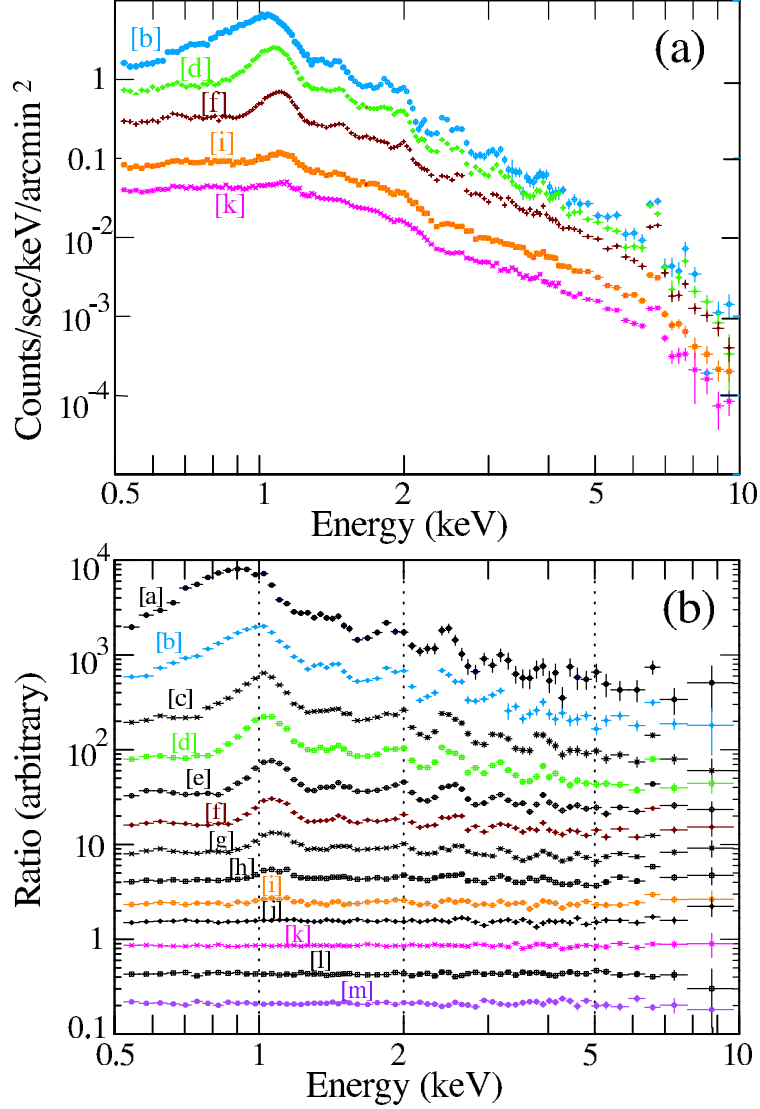


Fig. 2.— Background-subtracted EPIC-PN spectra of the Centaurus cluster extracted from annular regions (panel a), and their ratios to that averaged over the region of $5' < r < 12'$ (panel b). Outer radii used to extract the spectra are [a]10'', [b]25'', [c]40'', [d]1', [e]1'.5, [f]2', [g]3', [h]4', [i]5', [j]6', [k]8', [l]10', and [m]12'. The spectra are not corrected for the vignetting. In panel (a), only 5 out of the 13 spectra are shown for clarity. The ratios in panel (b) are vertically offset to avoid overlap.

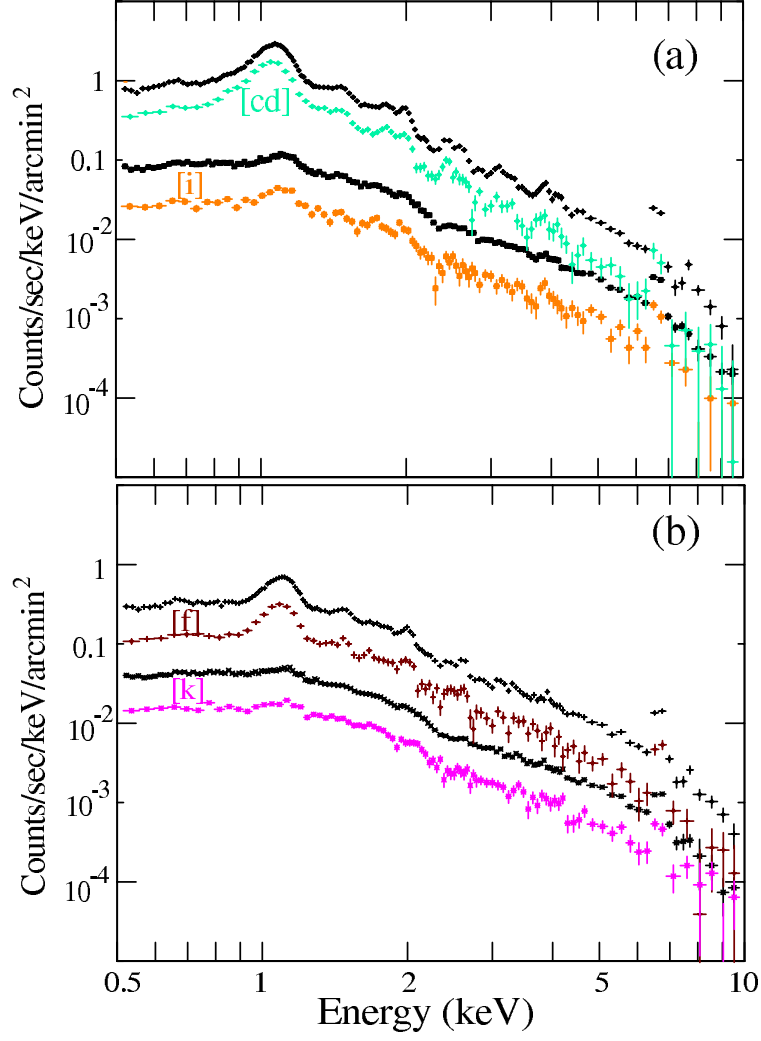


Fig. 3.— Deprojected PN spectra (colors) from concentric thin shells, compared with their non-deprojected counterparts (black). The regions used are; [cd]0'.5 – 1', [f]1'.5 – 2', [i]4' – 5', and [k]6' – 8'. To avoid heavy overlaps, a series of spectral pairs are shown on every other panel.

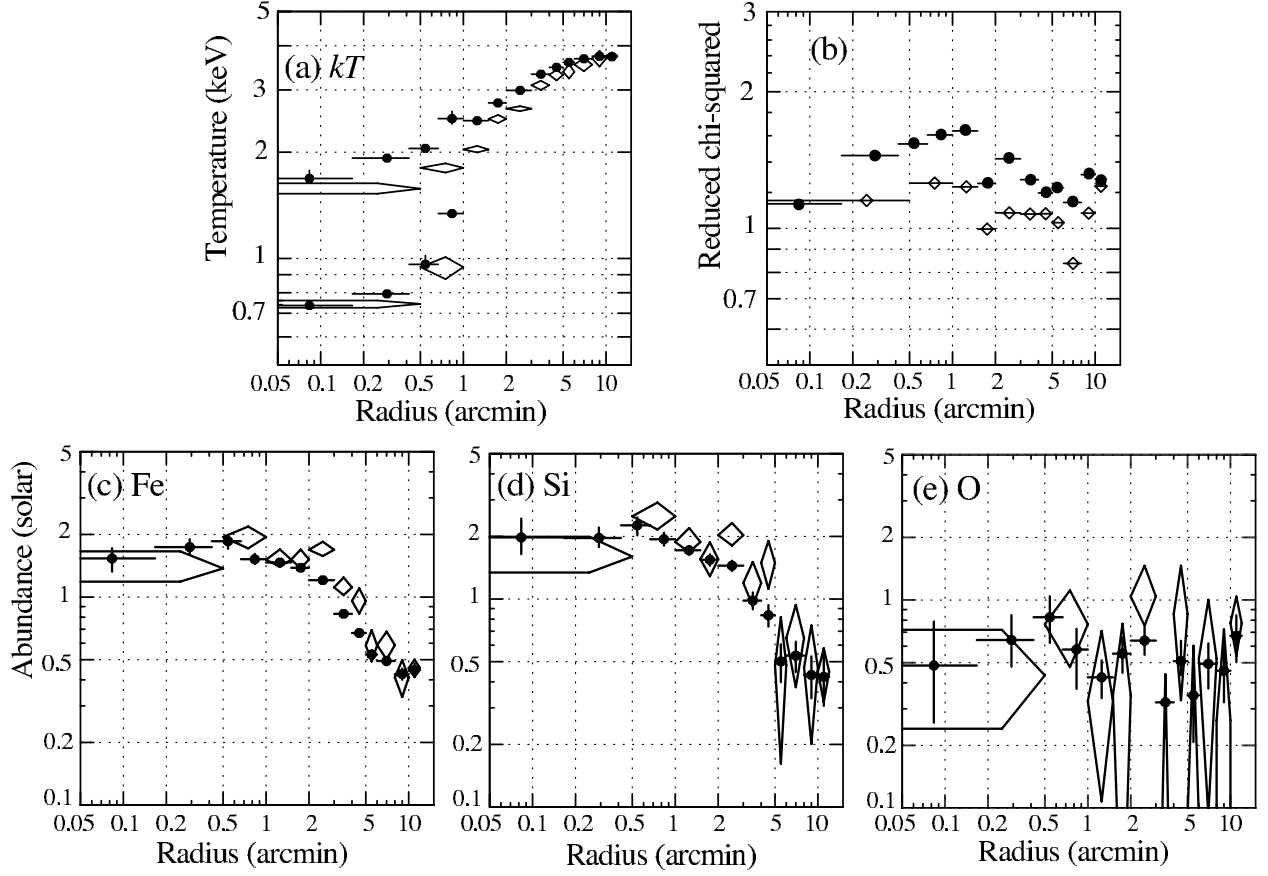


Fig. 4.— Radial profiles of (a) the temperature, (b) reduced chi-squared, and the abundances of (c) Fe, (d) Si, and (e) O of the Centaurus cluster, obtained with the 1P modeling. A ~ 0.7 keV component is added within $r < 1'$. Filled circles and open diamonds represent results from the non-deprojected and deprojected spectra, respectively.

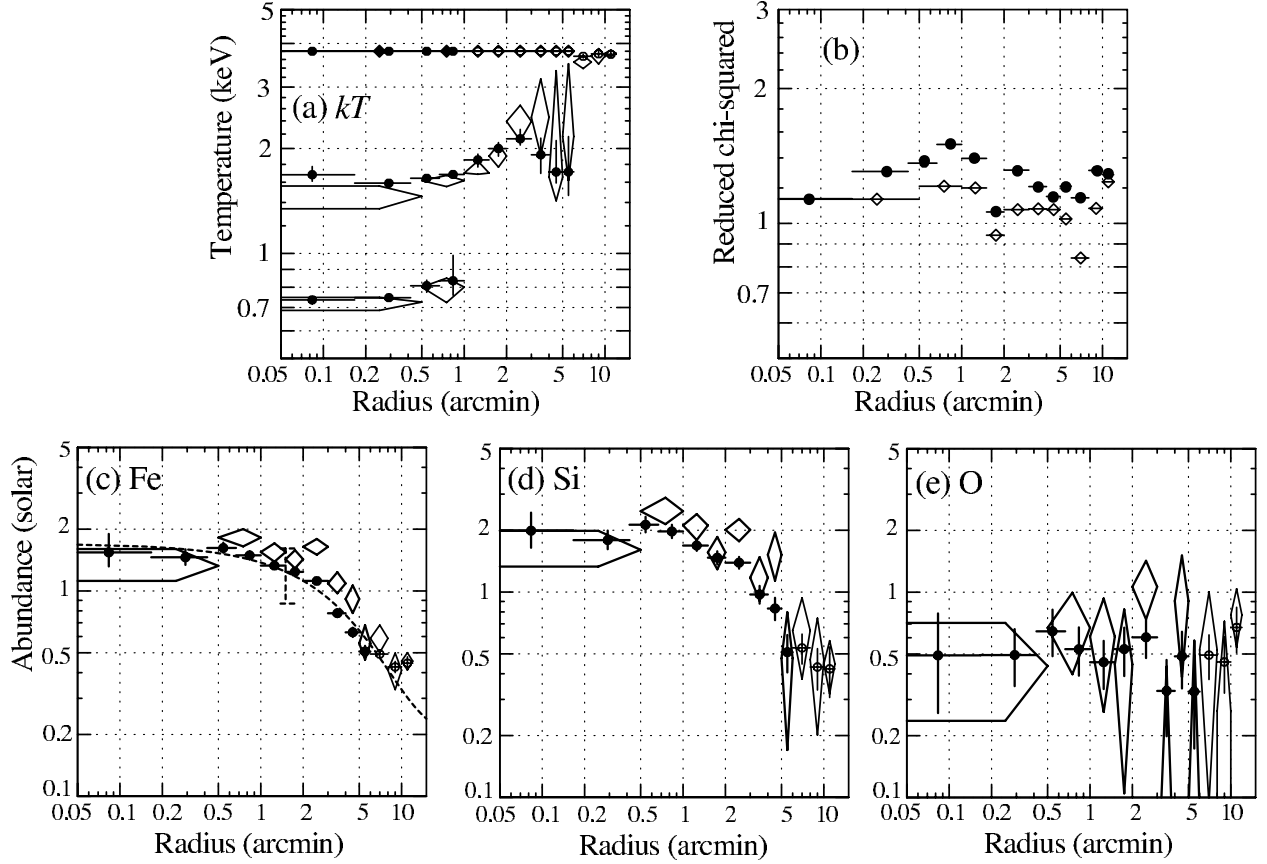


Fig. 5.— The same as Figure 4, but using the 2P model. The results outside $6'$, where the cool component is not required, are the same as those of Figure 4. In panel (c), the Fe abundance profile obtained with *ASCA* (Ikebe et al. 1999) is shown in the dashed line, together with its typical error size (30 %).

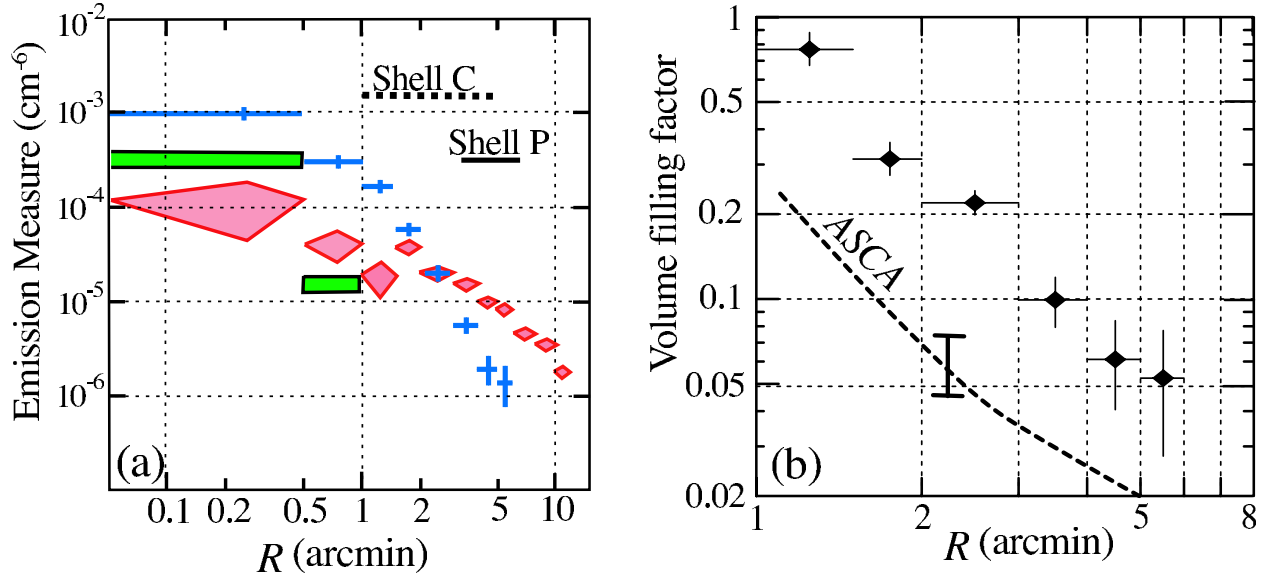


Fig. 6.— (a) Radial profiles of the emission measure per unit volume of the hot (red diamonds), cool (blue crosses), and the 0.7 keV (green squares) components, derived through the 2T fits to the deprojected EPIC spectra. Dashed and dotted horizontal lines indicate the radial ranges covered by Shell C and Shell P, respectively. (b) Radial profile of the volume filling factor of the cool component, calculated via eq.(5). That obtained with *ASCA* (Ikebe et al. 1999) is also shown with a dashed line, together with its typical error (25%).

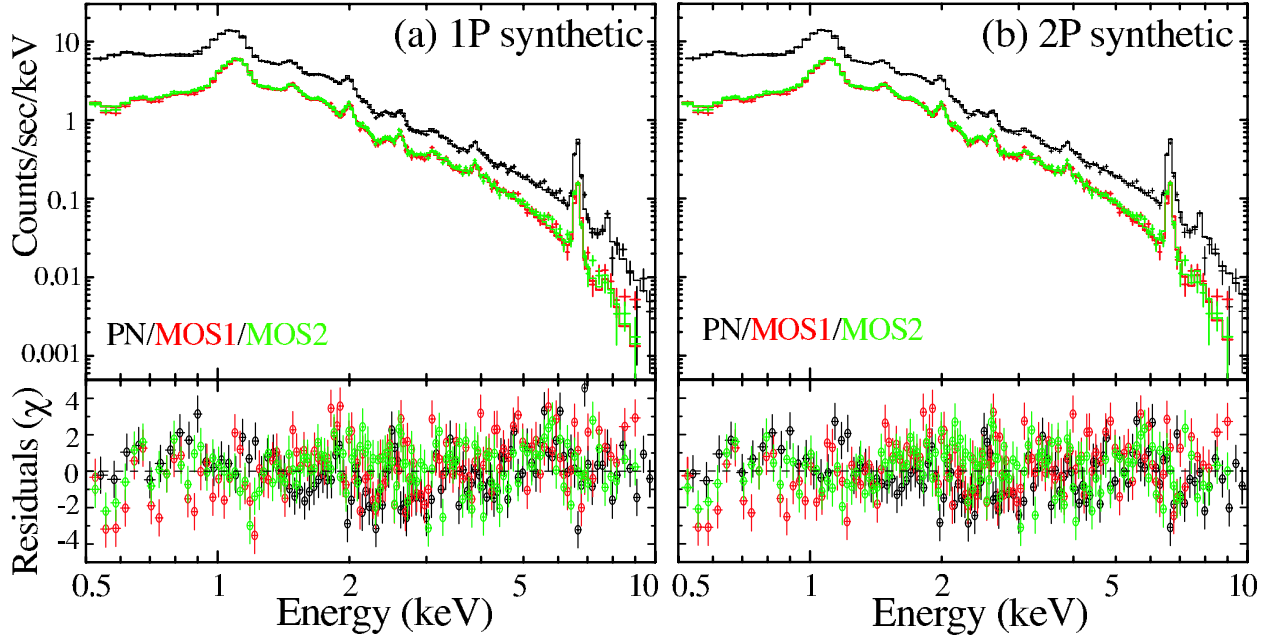


Fig. 7.— (a) Actual spectra from the thick Shell C, compared with the synthetic 1P model spectra (solid histograms) constructed from the best-fit 1P models to the constituent 5 thin-shell spectra (see text §4.2.2). The PN, MOS1, and MOS2 spectra are presented in black, red, and green, respectively. (b) The same Shell C spectra, fitted jointly with a simple 2P model of free temperatures and free abundances (§4.2.3). The fit goodness is summarized in Table 1.

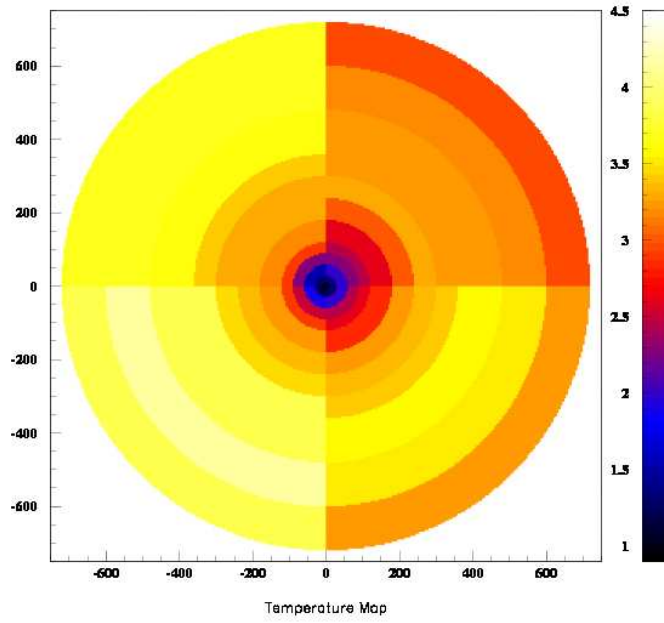


Fig. 8.— A temperature map of the Centaurus cluster, derived by analyzing the projected EPIC spectra in four azimuthal sectors and the 12 radial intervals. The MOS and PN spectra are fitted simultaneously by a 1P model (§ 4.1.2). The map scale is in units of arcsec, with north up and east to the left. The temperature color scale is in the unit of keV.

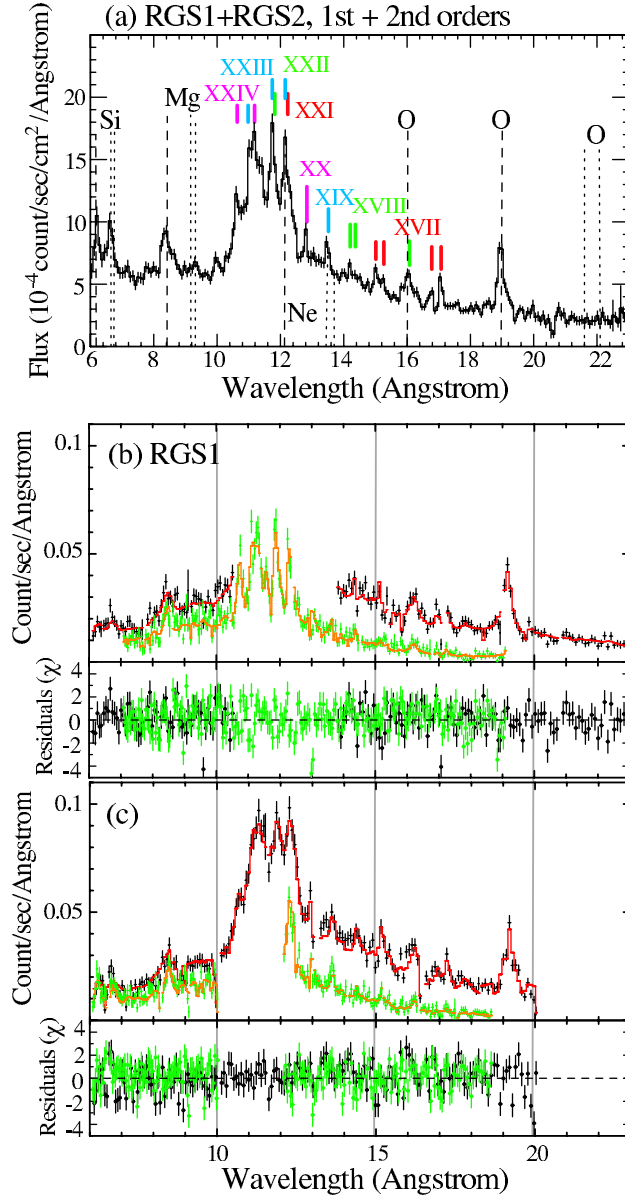


Fig. 9.— (a) Background-subtracted RGS flux spectrum made by combining four spectra, namely, the 1st and 2nd order spectra from the two RGS units. The positions of the H-like and He-like K-lines of several major elements are indicated with dashed and dotted lines, respectively. Color tick marks indicate Fe-L lines of various ionization states. (b) RGS1 spectra, fitted jointly with a 2P model. The first order spectrum and its model prediction are shown in black and red respectively, whereas the 2nd order data and its model predictions are in green and orange, respectively. (c) The same as panel (b), but for RGS2.

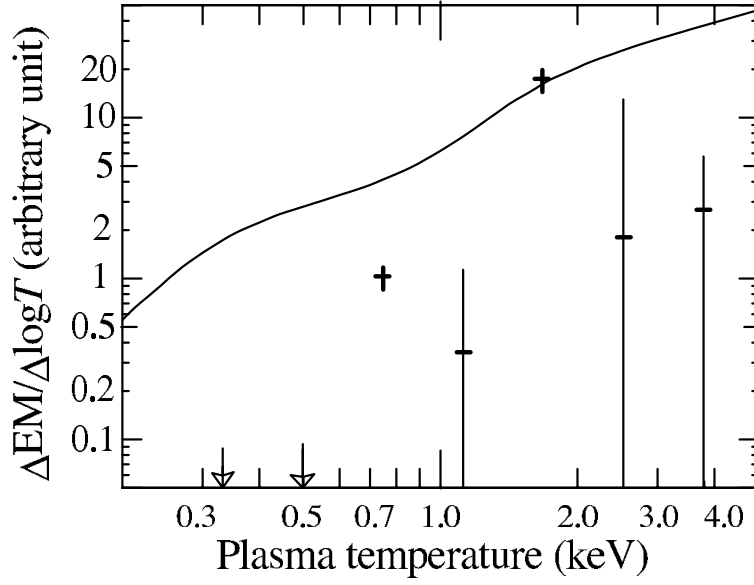


Fig. 10.— Distribution of the normalizations of individual temperature components, obtained with the multi temperature fit to the RGS data. The curve indicates the prediction by the isobaric cooling flow model, for plasmas of 1 solar abundances (Johnstone et al. 1992). The vertical scale is arbitrary.

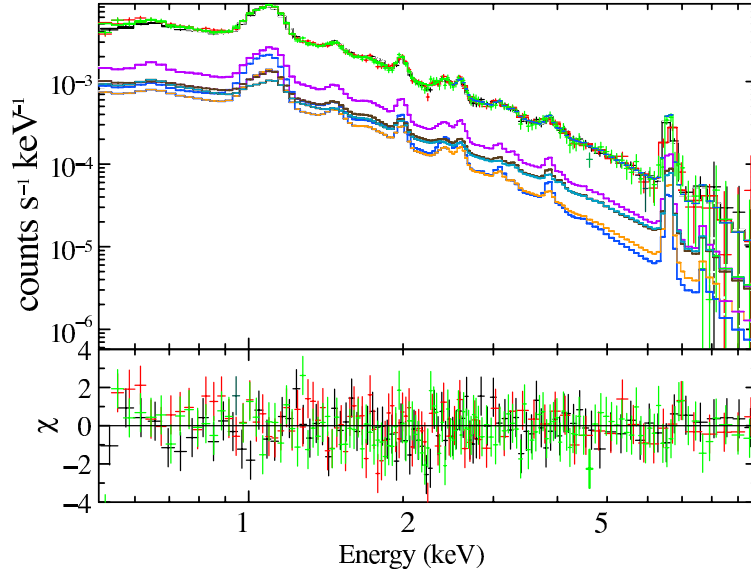


Fig. 11.— Spectra from Shell C of a simulated 1P cluster, compared with the convolved numerical models that are used to define the 5 constituent annular spectra (indicated only for MOS1 with different colors). The PN, MOS1, and MOS2 spectra are presented in black, red, and green, respectively. Their appearance differs from that of Fig. 7, simply because the energy-dependent effective areas, which are once removed in deprojection, are restored in Fig. 7 while not here for simplicity.

Table 1: Systematic uncertainties (1σ) assigned to the EPIC background data.

	band (keV)	errors	note
PN	< 1.35	8%	diffuse X-rays
	1.35–1.6	8%	Al line
	1.6–7.3	3%	
	7.3–9.2	8%	Ni, Cu, and Zn lines
	> 9.2	3%	
MOS	< 1.35	8%	diffuse X-rays
	1.38–1.85	8%	Al and Si lines
	> 1.85	3%	

Table 2: Summary of the fit goodness to the Shell C spectra.

Model	Condition	χ^2	ν	χ^2/ν	§§
1P	synthetic, no adjust.	739	378	1.96	4.2.2
	norm. adjusted	724	373	1.94	4.2.2
	revised sys. error	418	378	1.11	4.2.4
2P	simple 2P fit	688	363	1.90	4.2.3
	synthetic, no adjust.	678	378	1.79	4.2.3
	revised sys. error	381	378	1.01	4.2.4

Table 3: Results of the model fit to the RGS spectra.

Parameter	Comp. 1	Comp. 2
Temperature	$1.70^{+0.05}_{-0.03}$	$0.77^{+0.02}_{-0.04}$
Gaussian σ	$65''.8^{+5''.5}_{-5''.1}$	$19''.6^{+7''.9}_{-6''.8}$
Abundances (solar)		
O	0.39 ± 0.04	
Ne	0.60 ± 0.12	
Mg	$0.75^{+0.12}_{-0.13}$	
Si	$1.09^{+0.13}_{-0.12}$	
Fe	$0.75^{+0.04}_{-0.05}$	
Ni	$1.01^{+0.26}_{-0.25}$	
$\chi^2/\text{d.o.f.}$	985/727	